A&A 570, A76 (2014)
DOI: 10.1051/0004-6361/201424311

Astronomy & Astrophysics

High-resolution abundance analysis of red giants in the globular cluster NGC 6522⋆,⋆⋆

B. Barbuy[1], C. Chiappini[2], E. Cantelli[1], E. Depagne[2], M. Pignatari[3], R. Hirschi[4], G. Cescutti[2], S. Ortolani[5,6], V. Hill[7], M. Zoccali[8,9], D. Minniti[9,10], M. Trevisan[11], E. Bica[12], and A. Gómez[13]

[1] Universidade de São Paulo, IAG, Rua do Matão 1226, Cidade Universitária, 05508-900 São Paulo, Brazil
e-mail: barbuy@astro.iag.usp.br
[2] Leibniz-Institut für Astrophysik Potsdam (AIP), An der Sternwarte 16, 14482 Potsdam, Germany
e-mail: cristina.chiappini@aip.de
[3] Department of Physics, University of Basel, Klingelbergstrasse 82, 4056 Basel, Switzerland
[4] Astrophysics Group, Keele University, ST5 5BG, Keele, UK
[5] Dipartimento di Fisica e Astronomia, Università di Padova, 35122 Padova, Italy
[6] INAF-Osservatorio Astronomico di Padova, Vicolo dell'Osservatorio 5, 35122 Padova, Italy
[7] Laboratoire Lagrange (UMR7293), Université de Nice Sophia Antipolis, CNRS, Observatoire de la Côte d'Azur, CS 34229, 06304 Nice Cedex 4, France
[8] Universidad Catolica de Chile, Instituto de Astrofisica, Casilla 306, Santiago 22, Chile
[9] Millenium Institute of Astrophysics, Av. Vicuña Mackenna 4860, Macul, Santiago, Chile
[10] Departamento de Ciencias Fisicas, Universidad Andres Bello, Republica 220, Santiago, Chile
[11] Instituto Nacional de Pesquisas Espaciais, Av. dos Astronautas 1758, 12227-010 São José dos Campos, Brazil
[12] Universidade Federal do Rio Grande do Sul, Departamento de Astronomia, CP 15051, 91501-970 Porto Alegre, Brazil
[13] Observatoire de Paris-Meudon, GEPI, 92195 Meudon Cedex, France

Received 30 May 2014 / Accepted 31 July 2014

ABSTRACT

Context. The [Sr/Ba] and [Y/Ba] scatter observed in some galactic halo stars that are very metal-poor and in a few individual stars of the oldest known Milky Way globular cluster NGC 6522 have been interpreted as evidence of early enrichment by massive fast-rotating stars (spinstars). Because NGC 6522 is a bulge globular cluster, the suggestion was that not only the very-metal poor halo stars, but also bulge stars at [Fe/H] ∼−1 could be used as probes of the stellar nucleosynthesis signatures from the earlier generations of massive stars, but at much higher metallicity. For the bulge the suggestions were based on early spectra available for stars in NGC 6522, with a medium resolution of $R \sim 22\,000$ and a moderate signal-to-noise ratio.

Aims. The main purpose of this study is to re-analyse the NGC 6522 stars reported previously by using new high-resolution ($R \sim 45\,000$) and high signal-to-noise spectra ($S/N > 100$). We aim at re-deriving their stellar parameters and elemental ratios, in particular the abundances of the neutron-capture *s*-process-dominated elements such as Sr, Y, Zr, La, and Ba, and of the *r*-element Eu.

Methods. High-resolution spectra of four giants belonging to the bulge globular cluster NGC 6522 were obtained at the 8m VLT UT2-Kueyen telescope with the UVES spectrograph in FLAMES-UVES configuration. The spectroscopic parameters were derived based on the excitation and ionization equilibrium of Fe I and Fe II.

Results. Our analysis confirms a metallicity [Fe/H] = −0.95 ± 0.15 for NGC 6522 and the overabundance of the studied stars in Eu (with +0.2 < [Eu/Fe] < +0.4) and alpha-elements O and Mg. The neutron-capture *s*-element-dominated Sr, Y, Zr, Ba, and La now show less pronounced variations from star to star. Enhancements are in the range 0.0 < [Sr/Fe] < +0.4, +0.23 < [Y/Fe] < +0.43, 0.0 < [Zr/Fe] < +0.4, 0.0 < [La/Fe] < +0.35, and 0.05 < [Ba/Fe] < +0.55.

Conclusions. The very high overabundances of [Y/Fe] previously reported for the four studied stars is not confirmed with the new high-quality spectra. The moderate enhancement in [Sr/Fe] previously reported for one of the re-studied stars is confirmed, but the strong enhancements of this ratio for the other two stars are not confirmed. Despite the moderate enhancements found for the neutron-capture *s*-element-dominated species, none of the four stars studied here show positive values for all [Sr/Ba], [Y/Ba] and [Zr/Ba] ratios. The re-studied stars are now compatible not only with the interpretation that the *s*-process enhancements in these very old stars are due to spinstars, but also with alternative models such as mass transfer from *s*-process-rich AGB stars. Note, however, that when our results are interpreted in the context of more extended datasets from the literature, the spinstar scenario still seems to be favoured.

Key words. stars: abundances – stars: atmospheres – Galaxy: bulge – globular clusters: individual: NGC 6522

1. Introduction

The heavy-element abundances in very old stars have been interpreted by Truran (1981) to correspond to *r*-process products because the *s*-process enrichment cannot proceed promptly in the early Galaxy. On the other hand, it is well-known that rotation in massive stars can explain high primary nitrogen abundances in low-metallicity stars because of internal mixing induced by rotation (e.g. Barbuy 1983; Chiappini et al. 2006). It has now been shown that *s*-elements can also be produced in fast-rotating massive stars, or spinstars (Pignatari et al. 2008; Frischknecht et al. 2012). Chiappini (2013) described the impact

⋆ Observations collected at the European Southern Observatory, Paranal, Chile (ESO), under programmes 88.D-0398A.
⋆⋆ Appendix A is available in electronic form at http://www.aanda.org

of spinstars on the chemical enrichment of the early Universe, and how some of the very metal-poor halo data can be better matched when the spinstar's contribution is taken into account.

Chiappini et al. (2011, hereafter C11) reported the first *s*-process detailed nucleosynthesis calculations made by Frischknecht and collaborators for a fast-rotating massive star of 40 solar masses, with a metallicity [Fe/H] = −3.8 and rotational velocity $V_{\rm rot}$ = 500 km s^{-1}. It was shown that *s*-process elements in this star were boosted by up to four orders of magnitude with respect to a non-rotating star of same mass and metallicity (see their Fig. 2). An extended grid of spinstar models was later computed and published in Frischknecht et al. (2012). In particular, these calculations indicate an enhancement of the heavy elements Sr, Y, La, and Ba that are measurable in stellar spectra.

The yields of the first very metal-poor supernovae in the Galactic halo can be studied in the most metal-poor stars (e.g. Cayrel et al. 2004), whereas in the Galactic bulge a star formation rate enhanced by a factor 10 relative to the halo (e.g. Ballero et al. 2007) resulted in the oldest bulge stars having [Fe/H] ∼ −1.0 (Chiappini et al., in prep.). Evidence for the oldest bulge stellar populations having [Fe/H] ∼ −1.0 was reported in Lee (1992) and Dékány et al. (2013), in studies of bulge RR Lyrae with this metallicity. Also, a significant number of very old globular clusters with this metallicity was also found in the inner bulge (Minniti 1995; Rich et al. 1998; Barbuy et al. 2009, hereafter B09).

In C11 the stellar yields of the 40 solar mass spinstar were compared with the [Y/Ba] and [Sr/Ba] ratios observed in very metal-poor halo stars and with the abundances derived for red giant stars of the bulge metal-poor globular cluster NGC 6522. These abundances were first reported by B09. C11 suggested that bulge stars with a metallicity of [Fe/H] ∼ −1 might also hold information on the nature of the first generations of stars, as has been known to be the case for halo stars with metallicities below [Fe/H] ≃ −3 (e.g. Truran 1981; Cayrel et al. 2004). Although there are bulge stars with lower metallicities, the bulge metallicity distribution shows a sharp cutoff around [Fe/H] = −1 (e.g. Ness et al. 2014; Zoccali et al. 2008). Despite uncertainties in the NGC 6522 data, the eight stars measured showed a scatter in the [Y/Ba] ratio similar to that observed in very metal-poor halo stars (with [Fe/H] < −3).

In C11 it was then suggested that the highest values of the [Y/Ba] observed in the halo (around [Fe/H] = −3) and bulge (around [Fe/H] = −1) was caused by the *s*-process contribution of spinstars. Indeed, according to spinstar models, their production would be strongly dependent on mass and rotational-velocity, which would explain the observed scatter in the ratio of two chemical elements dominated by the *s*-process nucleosynthesis of two different *s*-process peaks. Although this explanation seemed unique for three stars of NGC 6522, other alternative explanations for stars with lower [Y/Ba] ratio at metallicities around [Fe/H] = −1 cannot be discarded, such as the asymptotic giant branch (AGB) mass-transfer contribution (Bisterzo et al. 2011). Moreover, it was also clear that the spinstar contribution is probably complementary to that coming from *r*-process nucleosynthetic sites (e.g. Goriely et al. 2013; Nakamura et al. 2013; Wanajo 2013; Qian 2012; Winteler et al. 2012; Arcones & Marínez-Pinedo 2011).

More recently, it was possible to quantitatively test these ideas for halo stars thanks to the more complete grid of spinstar stellar models provided in Frischknecht et al. (2012). With this grid we computed inhomogeneous chemical evolution models for the halo (Cescutti et al. 2013; Cescutti & Chiappini 2014) and showed that indeed the observed scatter in abundance ratios of two predominantly *s*-process elements in stars with metallicities between −4 < [Fe/H] < −3 can be well explained if the *s*-process contribution of spinstars in the early chemical enrichment of the Universe is considered. Aoki et al. (2013) proposed an alternative scenario for the scatter in [Sr/Ba]. Their suggestion is that the explosion of core collapse SNe could produce *r*-process, but in some cases the *r*-process-rich material is not ejected because of the subsequent collapse of the proton-neutron star to a black hole. On the other hand, there is currently no clear evidence from Galactic chemical evolution simulations that explosive primary processes alone can explain the observed distribution of [Sr/Ba] with respect to [Fe/H] in the Galactic halo, with an observed peak at about [Fe/H] ∼ −3, while this is the case for the *s*-process from spinstars (Cescutti & Chiappini 2014). This result is also confirmed taking into account a recent reanalysis of Sr observations in a large sample of metal-poor stars (Hansen et al. 2013). This peculiar feature of the *s*-process from spinstars is due to the intrinsic nature of the *s*-process in spinstars, which is not primary even though the main neutron source does not depend on the initial metallicity of the star (Pignatari et al. 2008; Frischknecht et al. 2012). For the bulge (Chiappini et al., in prep.), we instead find that the scatter in these abundance ratios is smaller, which is a consequence of the higher star formation rate. Interestingly, these new models cannot explain the large overabundances reported in B09 and C11. As we will show here, the new high-quality spectra analysed suggest lower [Sr/Ba] and [Y/Ba] than what was reported before based on FLAMES-GIRAFFE lower resolution spectra, and hence agree well with our model predictions.

We present results from new spectra obtained with the FLAMES-UVES spectrograph at the VLT, at a resolution R ∼ 45 000, and signal-to-noise ratio S/N ∼ 90−130 in the red portion (580−680 nm), and 70−130 in the blue portion (480−580 nm), to verify the previous abundance results. A detailed abundance analysis of four stars in NGC 6522 based on these higher resolution spectra is carried out using MARCS model atmospheres (Gustafsson et al. 2008).

The observations are described in Sect. 2. Photometric stellar parameters effective temperature and gravity are derived in Sect. 3. Spectroscopic parameters are derived in Sect. 4, and abundance ratios are computed in Sect. 5. A discussion is presented in Sect. 6 and conclusions are drawn in Sect. 7.

2. Observations

The spectra of individual stars of NGC 6522 were obtained at the VLT using the UVES spectrograph (Dekker et al. 2000) in FLAMES-UVES mode. The red chip (5800−6800 Å) has the ESO CCD#20, an MIT backside illuminated, of 4096 × 2048 pixels, and pixel size 15 × 15 μm. The blue chip (4800−5800 Å) uses the ESO Marlene EEV CCD#44, backside illuminated, of 4102 × 2048 pixels, and the pixel size is 15 × 15 μm. The UVES standard setup 580 yields a resolution R ∼ 45 000 for a slit width of 1 arcsec.The pixel scale is 0.0147 Å/pix, with ∼7.5 pixels per resolution element at 6000 Å.

The data were reduced using the UVES pipeline, within the ESO/Reflex software (Ballester et al. 2000; Modigliani et al. 2004). The log of the 2011−2012 observations is given in Table 1. The spectra were flatfielded, optimally extracted, and wavelength calibrated with the FLAMES-UVES pipeline. Spectra extracted from different frames were then co-added, taking into account the radial velocities reported in Table 2.

Table 1. Log of the spectroscopic observations carried out on October 8, 2011 (Julian Date 2 455 842), and 2012 March 6−7 and 25 (Julian Dates 2 455 992, 2 455 993, 2 456 011).

Date	UT	Exp (s)	Airmass	Seeing (″)
08.10.11	00:45:54.5	2750	1.328−1.595	0.82″
08.10.11	01:34:37.2	2750	1.611−2.096	1.29″
06.03.12	07:38:32.6	2750	1.743−1.414	1.15″
06.03.12	08:28:44.5	2750	1.343−1.176	0.93″
07.03.12	07:47:56.9	2750	1.630−1.348	0.81″
07.03.12	08:39:16.9	2750	1.372−1.167	0.73″
25.03.12	08:31:47.0	2750	1.127−1.048	0.64″

Notes. The quoted seeing is the mean value along the exposures on the detector.

Table 2. Radial velocities of the UVES sample stars, in each of the seven exposure runs with corresponding heliocentric radial velocities and mean heliocentric radial velocity.

Target	v_r^{obs}	$v_r^{hel.}$	Target	v_r^{obs}	$v_r^{hel.}$
	km s^{-1}	km s^{-1}		km s^{-1}	km s^{-1}
B-107 1	+21.705	−7.225	B-128 1	+14.745	−14.186
B-107 2	+21.594	−7.377	B-128 2	+14.559	−14.401
B-107 3	−37.038	−8.008	B-128 3	−43.743	−14.713
B-107 4	−36.955	−7.965	B-128 4	−43.725	−14.735
B-107 5	−36.715	−7.575	B-128 5	−43.990	−14.850
B-107 6	−36.705	−7.605	B-128 6	−43.928	−14.828
B-107 7	−37.440	−7.630	B-128 7	−44.657	−14.847
Mean	–	−7.626	Mean	–	−14.651
B-122 1	+11.333	−17.597	B-130 1	+12.351	−16.579
B-122 2	+11.156	−17.815	B-130 2	+12.105	−16.865
B-122 3	−47.488	−18.458	B-130 3	−46.004	−16.974
B-122 4	−47.500	−18.510	B-130 4	−46.049	−17.059
B-122 5	−47.059	−17.919	B-130 5	−45.779	−16.639
B-122 6	−47.133	−18.032	B-130 6	−45.849	−16.749
B-122 7	−47.778	−17.968	B-130 7	−46.601	−16.791
Mean		−18.043	Mean	–	−16.808

Previous observations by Zoccali et al. (2008) and B09 were taken in the wavelength range $\lambda\lambda$ 6100−6860 Å, using the GIRAFFE setups HR13 ($\lambda\lambda$ 6120−6402 Å), HR14 ($\lambda\lambda$ 6381−6620 Å), and HR15 ($\lambda\lambda$ 6605−6859 Å) at a resolution $R = 22\,000$ and $S/N = 80$−100.

The present UVES observations centred on 5800 Å yield a spectral coverage of $4800 < \lambda < 6800$ Å, with a gap at 5708−5825 Å. Five of the eight stars analysed in B09 and C11 were observed. The spectrum of B-108, however, appears to correspond to a much hotter star than in the early data (see detailed discussion in Sect. 5.2).

Table 3 gives the selected stars, their OGLE and 2MASS designations, coordinates, and the V, I magnitudes from the OGLE-II catalogue (Udalski et al. 2002) together with the 2MASS JHK$_s$ (Skrutskie et al. 2006) and VVV JHK$_s$ magnitudes (Saito et al. 2012).

3. Radial velocities

In Table 2 we report the radial velocities measured with IRAF/FXCOR for each of the seven runs, together with their mean values. A mean heliocentric radial velocity of $v_r^{hel} = -14.3 \pm 0.5$ km s^{-1} is obtained.

The radial velocities reported in B09 were revised. It was verified that the values given in B09 for setups HR14 and HR15 do not correspond to their radial velocities, given that these spectra had been shifted in wavelength, when they were reduced as presented in Zoccali et al. (2008). The observed radial velocities v_r were measured in each of the setups, and the HR14 and HR15 spectra were shifted to the same v_r zero point as that of HR13 (by means of an empirical differential heliocentric correction measured as the mean shift in radial velocity of all the stars, between a given setup and HR13). An average was taken as if all the spectra were taken on the same day as HR13. Then the heliocentric correction to v_r was calculated for the HR13 setups and was applied to all spectra. Therefore the v_r values from HR14 and HR15 given in B09 should be disconsidered, as well as the mean value of $v_r^{hel} = -24.9 \pm 0.7$ km s^{-1} given in B09.

The HR13 setup values given in B09 are the correct ones. Therefore the radial velocities are $v_r^{hel} = -6.59, -15.86, -12.28$, and -15.67 km s^{-1} for stars B-107, B-122, B128, and B-130 respectively. This results in a mean value of $v_r^{hel} = -12.6 \pm 0.7$ km s^{-1} for the GIRAFFE spectra, program 071.D-0617(A), that were studied in B09.

The present mean heliocentric radial velocity $v_r^{hel} = -14.3 \pm 0.5$ km s^{-1} found for NGC 6522 from the UVES spectra agrees well with the value $v_r^{hel} = -12.6 \pm 0.7$ km s^{-1} from the GIRAFFE data. It also agrees well with $v_r^{hel} = -18.3 \pm 9.3$ km s^{-1} reported by Rutledge et al. (1997a,b). A value of $v_r^{hel} = -28.5 \pm 6.5$ km s^{-1} was derived by Terndrup et al. (1998), and $v_r^{hel} = -21.1 \pm 3.4$ km s^{-1} is reported in the compilation by Harris (1996, updated in 2010)[1].

Finally, the variations of radial velocities given in Table 2 are within the errors, indicating that there is no evidence of binarity. In particular, the mass transfer from an AGB companion scenario, mentioned in Sect. 1, would be favoured in case of such evidence.

4. Photometric stellar parameters

4.1. Temperatures

The $VIJHK_s$ magnitudes are given in Table 3. V and I data of NGC 6522 were collected from the Optical Gravitational Lensing Experiment (OGLE) survey, the OGLE-II release, Field Bul-SC45 from Udalski et al. (2002), 2MASS J, H, and K_s from Skrutskie et al. (2006)[2] and J, H, and K_s from the Vista Variables in the Via Lactea survey (VVV, Saito et al. 2012). Note that for star B-130, the NASA/IPAC IRSA data base currently lists $J = 11.850$, but the previous value of $J = 12.850$, as given in B09, appears to be correct.

We adopted a reddening of $E(B-V) = 0.45$ according to the discussion in B09. Reddening laws from Dean et al. (1978) and Rieke & Lebofsky (1985), namely, $R_V = A_V/E(B-V) = 3.1$, $E(V-I)/E(B-V) = 1.33$, $E(V-K)/E(B-V) = 2.744$, $E(J-K)/E(B-V) = 0.527$, implying colour corrections of $A_I/E(B-V) = 1.77$, $A_J/E(B-V) = 0.88$, $A_H/E(B-V) = 0.55$, and $A_K/E(B-V) = 0.356$ were adopted.

Effective temperatures were derived from $V-I$, $V-K$, and $J-K$ using the colour-temperature calibrations of Alonso et al. (1999, hereafter AAM99). To transform $V-I$ from the Cousins to the Johnson system we use the relation $(V-I)_C = 0.778(V-I)_J$ (Bessell 1979). The J, H, K_S 2MASS magnitudes

[1] http://www.physics.mcmaster.ca/Globular.html
[2] http://ipac.caltech.edu/2mass/releases/allsky/

Table 3. Identifications, positions, and magnitudes. JHK_s from both the 2MASS and VVV surveys are given.

Star	OGLE No.	2MASS ID	α_{2000}	δ_{2000}	V	I	J	H	K_s	J_{VVV}	H_{VVV}	K_{VVV}
B-107	402361	18033660–3002164	18:03:36.59	–30:02:16.1	15.977	14.313	13.006	11.803	11.574	13.023	12.443	12.272
B-108	245265	–	18:03:35.19	–30:02:04.9	16.287	14.400	–	–	–	–	–	–
B-122	244582	18033338–3001588	18:03:33.35	–30:01:58.3	16.001	14.281	12.707	11.988	11.128	12.949	12.300	12.130
B-128	402607	18034463–3002107	18:03:44.62	–30:02:10.4	16.260	14.553	12.860	12.614	12.438	–	–	–
B-130	402531	18034102–3003036	18:03:41.01	–30:03:03.0	16.302	14.642	12.850	12.307	10.634	13.359	12.747	12.525

Table 4. Photometric stellar parameters derived using the calibrations by Alonso et al. (1999) for $V-I$, $V-K$, $J-K$, bolometric corrections, and bolometric magnitudes and the corresponding gravities log g, and final spectroscopic parameters.

	Photometric parameters								Spectroscopic parameters					
star	$T(V-I)$	$T(V-K)$ 2MASS	$T(J-K)$ 2MASS	$T(V-K)$ VVV	$T(J-K)$ VVV	BC_V	M_{bol}	log g	T_{eff}	log g	[FeI/H]	[FeII/H]	[Fe/H]	v_t
	(K)	(K)	(K)	(K)	(K)				(K)					km s^{-1}
B-107	4594	–	–	4664	4860	−0.37	0.97	2.50	4990	2.00	−1.11	−1.14	−1.12	1.40
									4900	2.10	−1.15	−1.06	−1.11	1.40
B-122	4487	–	–	4527	4621	−0.41	1.04	2.48	4900	2.7	−0.80	−0.82	−0.81	1.55
									4800	2.6	−0.87	−0.87	−0.87	1.10
B-128	4511	4572	6838	–	–	−0.40	1.28	2.58	4800	2.5	−0.81	−0.82	−0.81	1.25
									4800	2.7	−0.79	−0.79	−0.79	1.30
B-130	4602	4612	4773	4605	4586	−0.36	1.28	2.62	4850	2.2	−1.03	−1.05	−1.04	1.45
									4800	2.3	−1.09	−1.10	−1.09	1.40

Notes. For each star the last columns in the first line give the spectroscopic parameters from UVES spectra (present work), and the second line reports those derived from GIRAFFE spectra in B09.

and colours were transformed from the 2MASS system to that of the California Institute of Technology (CIT), and from this to that of the Telescopio Carlos Sánchez (TCS), using the relations established by Carpenter (2001) and Alonso et al. (1998). The VVV JHK_s colours were transformed to the 2MASS JHK_s system using relations reported by Soto et al. (2013). The derived photometric effective temperatures are listed in Table 4.

4.2. Gravities

Adopting $T_\odot = 5770$ K, $M_{bol\odot} = 4.75$, $M_* = 0.85\ M_\odot$ and a distance modulus of $(m-M)_0 = 13.91$, $A_V = 1.72$ (Barbuy et al. 1998), the following classical relation was used to derive gravities:

$$\log g_* = 4.44 + 4\log\frac{T_*}{T_\odot} + 0.4(M_{bol*} - M_{bol\odot}) + \log\frac{M_*}{M_\odot}.$$

The bolometric corrections from AAM99 and corresponding gravities are given in Table 4.

5. Spectroscopic stellar parameters

The equivalent widths (EW) were measured using the automatic code DAOSPEC that was developed by Stetson & Pancino (2008).

The EWs measured for the Fe I and Fe II lines are reported in Table A.5, where they are compared with values from B09. We restrained the list of Fe lines to those in the region 6100–6800 Å for the usual reasons of a higher S/N and a lower line crowding in this wavelength region, than in the region 4800–6100 Å. Another reason was the possibility of a more straightforward comparison of differences in the stellar parameters of B09. For star B-108 we also measured the lines of star B-108 using IRAF for a comparison. In Fig. A.1 we compare EWs from B09 and the present measurements, as well as their residuals. The EWs for stars B-107, B-122, B-128, and B-130 agree well within ±20 mÅ. For B-108 the values show a large scatter, which can be explained recalling that for this object two stars were included in the slit, as explained in Sect. 5.2. We also searched for a possible trend between EW and wavelength, but found none, except for lines in the region 6700–6800 Å, but since we only used lines with $30 < EW < 100$ mÅ, only very few EWs for lines in this region were used.

The error in EWs as given by Cayrel (1988) and Cayrel et al. (2004) is $\sigma = \frac{1.5}{S/N}\sqrt{FWHM * \delta x}$. We measured a mean $FWHM = 12.5$ pixels, or 0.184 Å. The CCD pixel size is 15 μm, or $\delta x = 0.0147$ Å in the spectra. By assuming a mean $S/N = 100$, we derive an error $\Delta EW \sim 0.8$ mÅ (note that this formula neglects the uncertainty in the continuum placement).

For the Fe I line list given in Table A.5, we employed the respective oscillator strengths described in Zoccali et al. (2004) and Barbuy et al. (2006, 2007).

Photospheric 1D models for the sample giants were extracted from the MARCS model atmosphere grid (Gustafsson et al. 2008). The LTE abundance analysis and the spectrum synthesis calculations were performed using the code described in Spite (1967), Cayrel et al. (1991), Barbuy et al. (2003), and Coelho et al. (2005). An iron abundance of ϵ(Fe) = 7.50 (Grevesse & Sauval 1998) was adopted. Molecular lines of CN ($A^2\Pi$-$X^2\Sigma$), C_2 Swan ($A^3\Pi$-$X^3\Pi$), TiO ($A^3\Phi$-$X^3\Delta$) γ, and TiO ($B^3\Pi$-$X^3\Delta$) γ' systems were taken into account.

The stellar parameters were derived by initially adopting the photometric effective temperature and gravity, and then further constraining the temperature by imposing an excitation equilibrium for the Fe I lines. Five Fe II lines were measurable, and their respective oscillator strengths from Biémont et al. (1991) were renormalized by Meléndez & Barbuy (2009). From this we derived gravities by imposing ionization equilibrium.

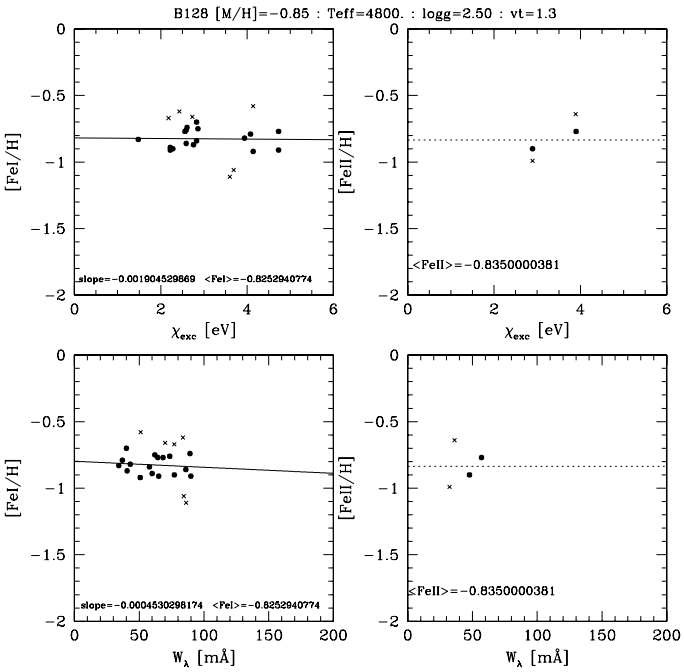

Fig. 1. Excitation and ionization equilibria of Fe I and Fe II lines for star B-128.

Microturbulence velocities v_t were determined by canceling the trend of Fe I abundance vs. equivalent width.

The final spectroscopic parameters $T_{\rm eff}$, $\log g$, [Fe I/H], [Fe II/H], [Fe/H], and the v_t values are reported in the last columns of Table 4. An example of excitation and ionization equilibria using the Fe I and Fe II lines is shown in Fig. 1 for star B-128. We preferred to use the spectroscopic parameters for consistency to fulfill the excitation and ionization equilibria of the Fe lines, even if overionization of Fe is expected, which might change these equilibria somewhat. The difference in abundances between Ti I and Ti II of 0.13 dex can be interpreted as having a too high effective temperature. We found spectroscopic temperatures systematically hotter by 200 K than the photometric temperatures (e.g. Zoccali et al. 2004).

In Table 4 a second line is added for each star, that lists the stellar parameters derived from GIRAFFE spectra in B09. The agreement is excellent, considering that the two derivations were made entirely independent of each other, with the only constraint of using the same list of Fe lines (with EWs measured from GIRAFFE and UVES).

5.1. Solar and Arcturus abundances

The lines were checked in the solar spectrum observed with the same instrumentation as the sample stars[3] and in the Arcturus spectrum (Hinkle et al. 2000). The solar abundances from the literature are given in Table 5. We adopted the Grevesse et al. (1998) abundances, which are similar to the latest abundances by Grevesse et al. (2014) or those by Lodders (2009). Literature parameters and abundances in Arcturus (α Boo, HR 5340, HD 124897, HIP 69673) are given in Table 6, with the parameters and abundances of the elements derived here for Arcturus reported in the last line of Table 6.

[3] http://www.eso.org/observing/dfo/quality/UVES/pipeline/solar-spectrum.html

Table 5. Solar *r*- and *s*-process fractions from Simmerer et al. (2004), and solar abundances from 1) Kurúcz (1993); 2) Grevesse et al. (1998); 3) Asplund et al. (2009); 4) Lodders (2009); 5) Grevesse et al. (2014).

El. Z	Fraction		$A(X)_\odot$				
	r	*s*	(1)	(2)	(3)	(4)	(5)
C 6	–	–	8.52	8.55	8.43	8.39	–
N 7	–	–	8.01	7.97	7.83	7.86	–
O 8	–	–	8.89	8.87	8.69	8.73	–
Na 11	–	–	6.29	6.33	6.24	6.30	–
Mg12	–	–	7.54	7.58	7.60	7.54	–
Al 13	–	–	6.43	6.47	6.45	6.47	–
Si 14	–	–	7.51	7.55	7.51	7.52	–
Ca 20	–	–	6.32	6.36	6.34	6.33	–
Ti 22	–	–	4.95	5.02	4.95	4.90	–
Fe 26	–	–	7.63	7.50	7.50	7.45	7.45
Sr 38	0.110	0.890	2.86	2.97	2.87	2.92	2.83
Y 39	0.281	0.719	2.20	2.24	2.21	2.21	2.21
Zr 40	0.191	0.809	2.46	2.60	2.58	2.58	2.59
Ba 56	0.147	0.853	2.09	2.13	2.18	2.18	2.25
La 57	0.246	0.754	1.18	1.17	1.10	1.14	–
Eu 63	0.973	0.027	0.47	0.51	0.52	0.52	0.52

Notes. Note: $A(X) = \log(X/H)+12$.

5.2. Star B-108

The star B-108 did not easily converge in terms of spectroscopic parameters. Therefore we investigated the star B-108 in detail, which was reported to have large heavy-element enhancements in C11.

We show in Fig. 2 the Advanced Camera for Surveys (ACS) of the *Hubble* Space Telescope (HST) image, taken on 10/07/2003, and superposed the size of the fibers of UVES and GIRAFFE, which are 1.″0 and 1.″2.

The sample star B-108 has no reported proper motions in the OGLE-II or in the UCAC4 (Zacharias et al. 2013) data bases. For the other sample stars the proper motions are of the order of 0.005 arcsec/yr, which are low enough not to change its location relative to the fiber size. From the ACS image it appears that the OGLE-II coordinates of star B-108 are shifted relative to its location. This is a warning not to use the coordinates directly but to verify images when possible. The image also shows that there is a blend of two stars. We examined the spectra in more detail, and in fact the asymmetry of lines reveals spectra of two stars of similar radial velocity, but with a small difference, as exemplified in Fig. 3.

The lower resolution of GIRAFFE caused a misanalysis of star B-108 in B09, while the UVES higher resolution which permits a better deblending of the spectra of the two stars, led to a less satisfactory set of parameters.

B-108 was finally discarded from the sample because o a clear contamination of its spectrum, and previous abundances of this star cannot be considered. It would be useful to observe both of these blended stars and determine whether the abundance enhancements detected in C11 are present.

6. Abundance ratios

Abundance ratios were obtained by means of line-by-line spectrum synthesis calculations that were compared with the observed spectra, for the line lists given in Tables 8, 9, and 11.

Table 6. Parameters employed for Arcturus, which was used as a reference star.

$T_{\rm eff}$	log g	$v_{\rm t}$	[Fe/H]	[O/Fe]	[Ca/Fe]	[Sr/Fe]	[Y/Fe]	[Zr/Fe]	[Ba/Fe]	[La/Fe]	[Eu/Fe]	Ref.
4260	0.90	–	–0.70	+0.10	+0.25	–0.40	–0.30	–0.20	–0.25	–0.20	–0.15	1
4280	1.30	1.40	–0.54	–	+0.17	–	–0.42	–1.07	+0.16	–0.15	+0.32	2
4300	1.50	1.70	–0.50	+0.40	+0.30	0.0	0.0	0.0	0.0	0.0	0.0	3
4350	1.60	1.60	–0.56	–	–	–0.27	–0.08	–0.07	–	–0.15	+0.15	4
4350	1.60	1.60	–0.58	–	+0.26	–0.17	–0.01	–	–0.07	–0.02	+0.39	5
4340	1.93	1.87	–0.55	+0.60	–0.01	–	–0.07	–	–0.28	–0.01	+0.21	6
4275	1.55	1.65	–0.54	+0.39	+0.28	–0.3	–0.3	–0.07	–0.30	–0.30	+0.15	7

References. 1) Mäckle et al. (1975); 2) McWilliam & Rich (1994); 3) Peterson et al. (1993); 4) Gopka et al. (2001); 5) Mishenina et al. (2001, 2003); 6) Luck & Heiter (2005); 7) parameters from Meléndez et al. (2003) and abundances from the present work.

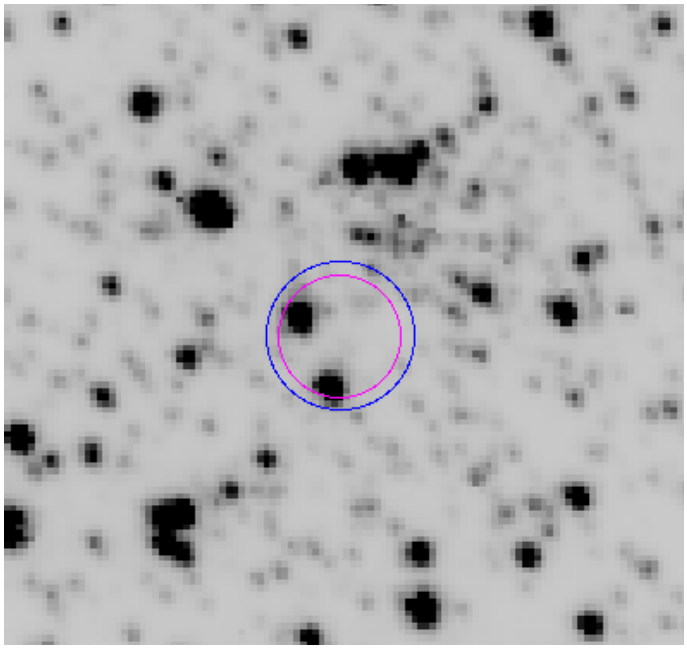

Fig. 2. ACS image of B-108. The circles indicate the size of the UVES and GIRAFFE fibers: two stars are present.

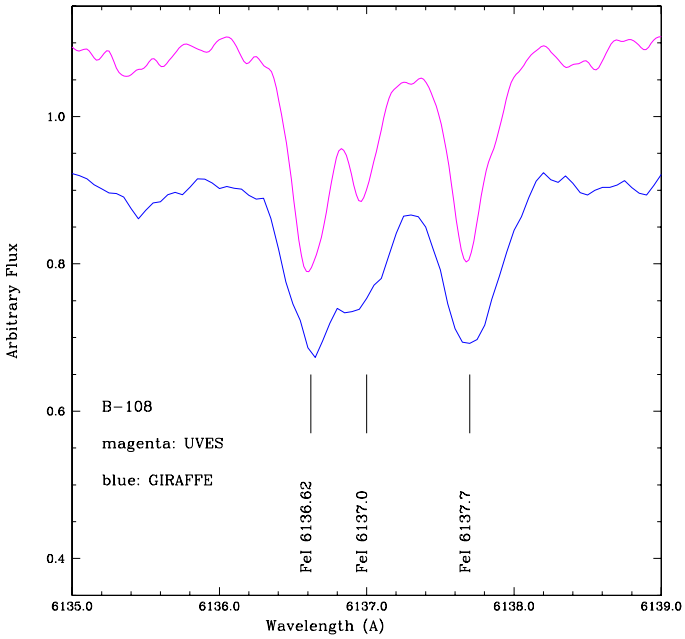

Fig. 3. UVES and GIRAFFE spectra of star B-108. The lines show two components of superposed spectra of the two stars. The two components are indicated by the asymmetry of the line profiles.

6.1. Carbon, nitrogen, and oxygen

The carbon abundances were estimated from the C_2(0,1) bandhead at 5635.3 Å. The fit to B-122 is shown in Fig. 4. Since the bandhead is extended, as can be seen in Fig. 4, a mean value was deduced from the overall fit, but giving more weight to the bandhead. The list of C_2 lines is the laboratory list from Phillips & Davis (1968). The resulting C and N abundances are given in Table 7.

The forbidden oxygen line [OI] 6300.311 Å in B-128 and B-130 can be detected on the right side of a telluric line. The same is true for B-122, but the oxygen line is weaker. To examine this we overplotted the spectrum of a B star with high rotation that shows a continuum with the telluric lines in it. For B-107 there is no blend with a telluric line, but the oxygen line appears anomalously strong.

The [OI] 6363.776 Å line has the advantage of not being masked by telluric lines, but the disadvantage of being weaker and blended on the blue side by a FeI line.

The nitrogen abundances were measured using the CN (5, 1) 6332.18 Å and CN (6, 2) 6478.48 Å of the CN $A^2\Pi$-$X^2\Sigma$ red system. The CN(5, 1) bandhead in star B-128 is shown in Fig. 5.

We iteratively recomputed the abundances in a sequence C, O, and N because the N abundance is very sensitive to the C abundance in CN molecules, and O is sensitive to C abundances because of the CO formation.

Table 7. C and N abundances from C_2 and CN bandheads.

Species	λ (Å)	B-107	B-122	B-128	B-130
C_2(0, 1)	5635.3	∼0.0	≤−0.2	∼0.1	∼0.0
CN(5, 1)	6332.16	–	≤0.7	∼0.7	∼0.7:
CN(6, 2)	6478.48	–	≤0.7	∼0.5	∼0.7

The results show a low carbon [C/Fe] < 0.1 for all stars, enhanced nitrogen, as expected in giants, and enhanced oxygen 0.2 < [O/Fe] < 0.5, typical of enrichment by SNe type II.

6.2. Odd-Z elements Na, Al, and alpha elements

In Table 8 we report the line-by-line α-element and odd-Z element abundances for the same line list as in B09, which essentially agrees well for the two abundance derivations. In Table 9 we report a complementary list of lines in the wavelength region 4800−6100 Å, now available with the UVES spectra. This bluer line region is subject to more blending lines however, and is therefore less reliable. We list oscillator strengths from the

Table 8. Abundance ratios [X/Fe] of alpha-elements O, Mg, Si, Ca, Ti, and odd-Z Na, Al, and atomic parameters adopted.

Species	λ (Å)	χ_{ex} (eV)	log gf	[X/Fe]							
				B-107	B-107b	B-122	B-122b	B-128	B-128b	B-130	B-130b
OI	6300.311	0.00	−9.716	–	>0.5:	–	+0.3:	–	+0.30	+0.5:	+0.50
OI	6363.776	0.00	−10.25	+0.5:	+0.5:	+0.7:	+0.2	+0.7:	+0.15	–	+0.50
NaI	6154.230	2.10	−1.56	−0.30	−0.20	+0.10	−0.10	+0.10	0.00	+0.10	0.00
NaI	6160.753	2.10	−1.26	−0.30	0.00	+0.20	−0.10	+0.10	+0.10	+0.20	+0.05
MgI	6318.720	5.11	−2.10	+0.20	+0.30	+0.20	+0.20	+0.20	+0.30	+0.40	+0.30
MgI	6319.242	5.11	−2.36	–	+0.30	+0.20	+0.10	+0.20	+0.30	+0.40	+0.30
MgI	6319.490	5.11	−2.80	+0.20	+0.30	+0.20	+0.10	+0.40	+0.40	+0.40	–
MgI	6765.450	5.75	−1.94	+0.40	–	–	–	+0.20	0.00	+0.40	–
SiI	6142.494	5.62	−1.50	+0.20	+0.20	0.00	0.00	+0.20	+0.30	+0.40	–
SiI	6145.020	5.61	−1.45	+0.20	+0.05	+0.20	0.00	+0.20	+0.30	–	–
SiI	6155.142	5.62	−0.85	+0.1	+0.05	−0.1	0.00	+0.20	+0.15	+0.30	+0.15
SiI	6237.328	5.61	−1.01	+0.20	+0.20	+0.20	+0.20	+0.30	+0.10	+0.40	+0.15
SiI	6243.823	5.61	−1.30	+0.20	+0.20	+0.30	0.00	+0.4	0.00	+0.40	+0.15
SiI	6414.987	5.87	−1.13	+0.20	+0.20	+0.20	0.00	+0.20	+0.20	+0.20	+0.15
SiI	6721.844	5.86	−1.17	+0.30	0.00	–	0.00	+0.20	+0.30	+0.40	+0.15
CaI	6156.030	2.52	−2.39	+0.30	+0.30	0.00	+0.30	+0.30	+0.30	–	+0.30
CaI	6161.295	2.51	−1.02	0.00	+0.15	+0.30	0.00	+0.20	+0.30	+0.30	+0.20
CaI	6162.167	1.89	−0.09	+0.20	+0.15	0.00	0.00	0.00	0.00	+0.10	0.00
CaI	6166.440	2.52	−0.90	0.00	0.00	+0.30	−0.05	0.00	0.00	+0.30	0.00
CaI	6169.044	2.52	−0.54	+0.10	+0.25	+0.30	−0.05	+0.30	+0.30	+0.10	0.00
CaI	6169.564	2.52	−0.27	+0.20	+0.10	+0.30	0.00	+0.30	+0.30	+0.20	0.00
CaI	6439.080	2.52	+0.3	+0.30	+0.25	+0.30	0.00	+0.30	+0.30	+0.30	+0.30
CaI	6455.605	2.52	−1.35	0.00	+0.10	+0.30	+0.10	−0.10	+0.10	+0.40	+0.30
CaI	6464.679	2.52	−2.10	0.00	+0.30	+0.30	+0.30	+0.30	+0.30	—	–
CaI	6471.668	2.52	−0.59	0.00	0.00	+0.30	0.00	+0.30	+0.30	+0.30	+0.20
CaI	6493.788	2.52	0.00	−0.30	+0.15	0.00	0.00	0.00	+0.30	+0.10	+0.30
CaI	6499.654	2.52	−0.85	−0.30	–	0.00	–	0.00	–	+0.10	–
CaI	6572.779	0.00	−4.32	0.00	+0.10	+0.20	0.00	0.0	0.00	+0.20	+0.10
CaI	6717.687	2.71	−0.61	0.00	+0.15	+0.30	0.00	+0.30	+0.20	+0.30	+0.10
TiI	6126.224	1.07	−1.43	+0.20	+0.10	+0.10	0.00	+0.10	0.00	+0.20	0.00
TiI	6258.110	1.44	−0.36	0.00	+0.15	+0.20	0.00	+0.20	0.00	0.00	0.00
TiI	6261.106	1.43	−0.48	0.00	0.00	+0.30	0.00	0.00	0.00	0.00	0.00
TiI	6303.767	1.44	−1.57	0.00	0.00	+0.20	+0.30	+0.20	+0.30	–	0.00
TiI	6336.113	1.44	−1.74	–	0.00	+0.30	0.00	0.00	–	–	–
TiI	6554.238	1.44	−1.22	+0.20	–	+0.20	0.00	+0.20	0.00	0.00	0.00
TiI	6556.077	1.46	−1.07	+0.20	–	0.00	0.00	+0.20	0.00	+0.40	0.00
TiI	6599.113	0.90	−2.09	+0.30	–	+0.20	+0.20	+0.20	+0.20	+0.40	+0.20
TiI	6743.127	0.90	−1.73	+0.10	0.00	0.00	0.00	0.0	0.00	+0.20	0.00
TiII	6491.580	2.06	−2.10	+0.30	+0.40	+0.30	+0.30	+0.30	+0.30	+0.30	+0.30
TiII	6559.576	2.05	−2.35	0.00	+0.30	+0.30	+0.30	+0.30	+0.30	+0.30	+0.30
TiII	6606.970	2.06	−2.85	+0.20	+0.20	–	0.00	+0.30	+0.30	+0.30	–

Notes. Column 4 reports the log gf adopted as described in B09. For each star the left column reports the results from B09 and the right column gives the present results.

literature and the adopted values based on fits to the solar spectrum observed with the UVES spectra as done in Sect. 3.1.

Table 10 lists the final abundance results from Tables 8 and 9.

Odd-Z elements Na, Al

We inspected the abundance results as a function of effective temperature and microturbulence velocity. The abundances of odd-*Z* elements Na and Al show a trend vs. effective temperature, which was corrected for. The corrected values are given in parenthesis in Table 10. For the other elements there is no evidence of a significant trend.

Alpha elements

The "bona-fide" α-elements in terms of nucleosynthesis production by SNe type II, O, and Mg, are enhanced in the four sample stars. Silicon is moderately enhanced, and Ca is moderately enhanced in two stars and is solar in one star. As for Ti, TiII gives moderate enhancements, while TiI gives solar ratios, and for both we find a mean low enhancement of +0.05 < [Ti/Fe] < +0.1.

The results in B09 of [O/Fe] = +0.4, [Mg/Fe] = +0.3, [Si/Fe] = +0.3, [Ca/Fe] = +0.2, [Ti/Fe] = +0.3, are the same as here for O and Mg, but we find lower enhancements for Si, Ca, Ti, of [Si/Fe] = +0.15, [Ca/Fe] = +0.10 and [Ti/Fe] = +0.15.

Na-O anticorrelation

A Na-O anticorrelation was clearly made evident in many globular clusters, most likely caused by material processed in the Ne-Na cycle of proton capture reactions. The expectation is that O is depleted and Na and Al are enhanced. (e.g. Gratton et al. 2012 and references therein). For this reason, we compared the present Na and O abundances with those for the globular cluster NGC 6121, with a metallicity of [Fe/H] = −1.16, which is similar to NGC 6522. The values of [Na/Fe] vs. [O/Fe] with abundances derived for 14 stars of NGC 6121 by Carretta et al. (2009) are plotted in Fig. 6. The present results are plotted with

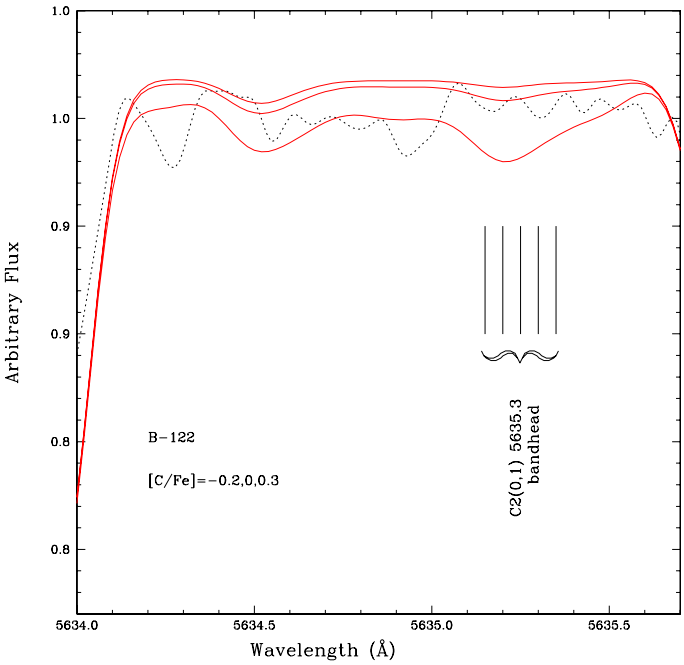

Fig. 4. $C_2(1,0)$ bandhead at 5635.3 Å in B-122.

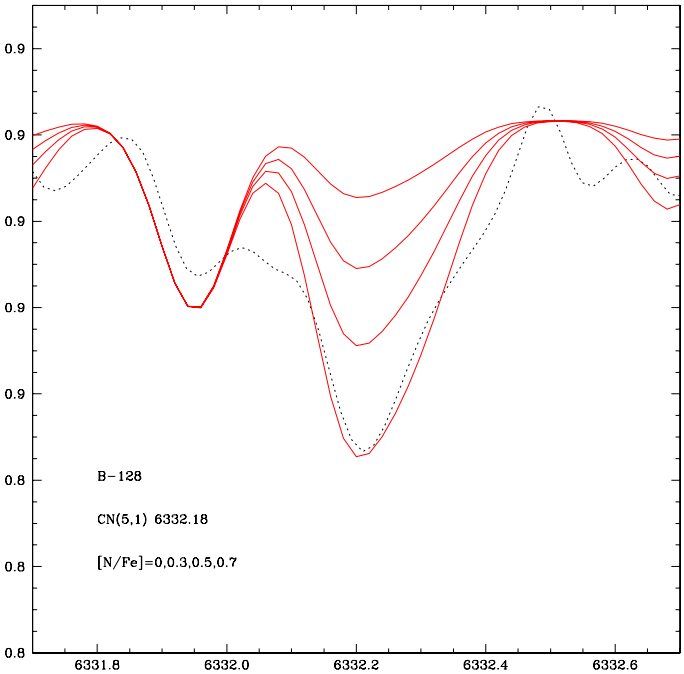

Fig. 5. Star B-128: CN(5, 1) bandhead at 6332.18 Å.

the original Na abundance derivation, and the values were corrected as explained above.

The four sample stars have [Na/Fe] ∼ 0 and do not seem to show a Na-O anticorrelation, differently from NGC 6121 and many other clusters, as shown by Carretta et al. (2009). More stars are needed to arrive at definitive conclusions. Since the stars in our sample share the same Na enrichment, we may conclude that they belong to the same generation within the cluster. The rather low [Na/Fe] ratio indicates that probably they all belong to a first generation of stars.

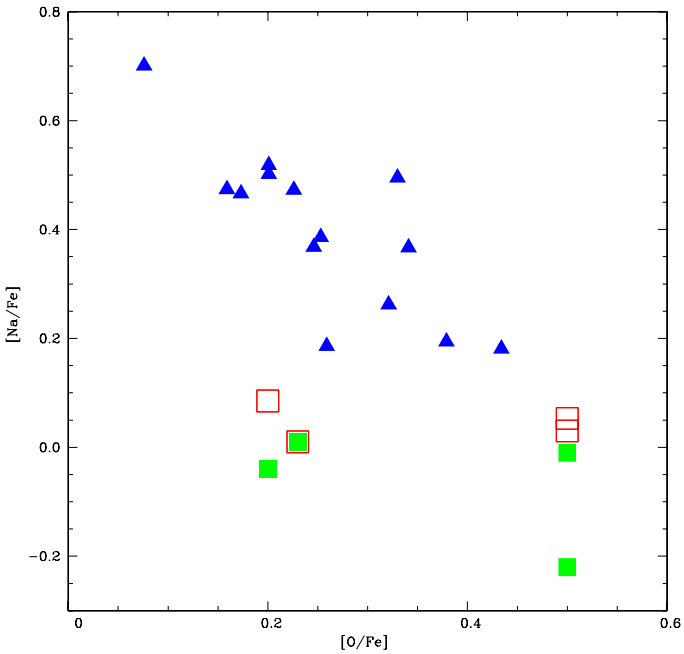

Fig. 6. [Na/Fe] vs. [O/Fe] for the sample stars compared with stars of NGC 6121. Symbols: blue filled triangles: stars of NGC 6121; (Na, O) for the sample stars: **a)** green filled squares: [Na/Fe] not corrected; **b)** open red squares: [Na/Fe] corrected.

6.3. Heavy elements

We derive the abundances of the neutron-capture elements Sr, Y, Zr, La, and Ba and the reference *r*-element Eu.

For the heavy elements Sr, Y, Zr, La, Ba, and Eu, the first ionization stages dominate the total abundances in the studied effective temperature range ($4000 < T_{\rm eff} < 6000$ K), therefore we preferentially used lines of ionized species. Because of a lack of reliable ionized lines, we also measured abundances from lines of Sr I, Y I, and Zr I.

We checked the solar and Arcturus spectra for lines of these elements by computing synthetic spectra and verifying the change in their intensities that is due to changes in abundances. The lines were selected when their contribution to the line in question was dominant, as well as by checking which of them were present and measurable in the sample stars, even if in some cases they are too faint in the solar and/or Arcturus spectra.

The wavelengths, excitation potentials, and oscillator strengths were gathered from the line lists of the Kurúcz (1993) websites[4,5], the National Institute of Standards & Technology (NIST, Martin et al. 2002)[6], and VALD (Piskunov et al. 1995).

The hyperfine structure (HFS) for the studied lines of La II, Ba II, and Eu II were taken into account. We computed the splitting of lines by employing a code made available by Andrew McWilliam, following the calculations described by Prochaska & McWilliam (2000).

Barium: the nuclear spin is $I = 1.5$ and the nuclides ^{138}Ba and ^{137}Ba, Ba^{136}, Ba^{135} and Ba^{134} contribute with 71.7%, 11.23%, 7.85%, 6.59%, and 2.42% to the total abundance respectively (Lodders 2009). Experimental data on hyperfine coupling constants, the magnetic dipole A-factor, and the electric

[4] http://www.cfa.harvard.edu/amp/ampdata/kurucz23/sekur.html
[5] http://kurucz.harvard.edu/atoms.html
[6] http://physics.nist.gov/PhysRefData/ASD/lines_form.html

Table 9. Central wavelengths from NIST or Kurúcz line lists and total oscillator strengths from line lists by Kurúcz, NIST, and VALD, the literature, and adopted values.

Species	λ (Å)	χ_{ex} (eV)	gf_{Kurucz}	gf_{NIST}	gf_{VALD}	$gf_{literature}$	$gf_{adopted}$	B-107	B-122	B-128	B-130
NaI	5682.6333	2.102439	−0.700	−0.706	−0.860	−0.66[1]	−0.706	−0.30	0.00	−0.05	−0.10
NaI	5688.2046	2.104571	−0.450	−0.452	−0.320	−0.28[1]	−0.45	−0.30	0.00	0.00	0.00
NaI	5688.1940	2.104571	−1.400	–	–	–	−1.400	−0.30	0.00	0.00	0.00
AlI	6696.185	4.021753	−1.576	−1.342	−0.320	−1.45[1]	−1.576	−0.30	−0.20	+0.10	0.00
AlI	6696.788	4.021919	−1.421	−1.342	−0.320	−1.45[1]	−1.421	−0.30	−0.20	+0.10	0.00
AlI	6696.788	4.021919	−2.722	−1.342	−0.320	−1.45[1]	−2.722	−0.30	−0.20	+0.10	0.00
AlI	6698.673	3.142933	−1.647	–	−0.320	−1.78[1]	−1.647	−0.30	−0.20	0.00	0.00
MgI	5528.4047	4.346096	−0.620	−0.498	−0.620	−0.25[1]	−0.498	+0.40	0.00	+0.15	+0.20
SiI	5665.555	4.920417	−2.040	−2.040	−2.04	−1.94[1]	−2.04	+0.20	+0.15	0.00	+0.15
SiI	5666.690	5.616073	−1.050	–	−1.795	−1.74[1]	−1.74	+0.30	+0.15	0.00	+0.15
SiI	5690.425	4.929980	−1.870	−1.870	−1.870	−1.75[1]	−1.87	+0.20	+0.15	+0.10	+0.20
SiI	5948.545	5.082689	−1.230	−1.231	−1.230	−1.17[1]	−1.30	+0.30	0.00	0.00	+0.30
CaI	5601.277	2.525852	−0.690	−0.69	−0.523	−0.52[1]	−0.52	0.00	−0.30	+0.00	+0.20
CaI	5867.562	2.932710	−0.801	–	−1.570	−1.58[1]	−1.55	0.0	0.0	+0.3	+0.3
CaI	6102.723	1.879467	−0.890	−0.79	−0.793	−0.65[1]	−0.793	0.00	0.00	0.00	+0.05
CaI	6122.217	1.885935	−0.409	−0.315	−0.316	−0.02[1]	−0.20	0.00	−0.30	+0.30	0.00
TiI	5689.459	2.296971	−0.469	−0.36	−0.360	−0.45[1]	−0.40	0.00	0.00	0.00	0.00
TiI	5866.449	1.066626	−0.840	−0.840	−0.840	−0.71[1]	−0.84	0.0	0.0	+0.15	0.00
TiI	5922.108	1.046078	−1.466	−1.465	−1.466	−1.47[1]	−1.46	0.00	0.00	0.00	0.00
TiI	5941.750	1.052997	−1.510	−1.52	−1.51	−1.54[1]	−1.53	+0.15	0.00	0.00	+0.10
TiI	5965.825	1.879329	−0.409	−0.409	−0.409	−0.50[1]	−0.42	0.00	+0.10	+0.10	+0.05
TiI	5978.539	1.873295	−0.496	−0.496	−0.496	−0.51[1]	−0.53	0.0	0.0	0.0	+0.2
TiI	6064.623	1.046078	−1.944	−1.944	−1.944	−1.89[1]	−1.944	0.00	−0.05	0.00	0.00
TiI	6126.214	1.066626	−1.425	−1.424	−1.425	−1.33[1]	−1.425	0.00	0.00	0.00	0.00
TiII	5154.0682	1.565869	−1.920	−1.92	−1.750	−1.60[1]	−1.75	0.00	0.00	0.00	0.00
TiII	5336.771	1.581911	−1.700	−1.70	−1.59	−1.54[1] , −1.60[2]	−1.70	0.00	0.00	0.00	0.00
TiII	5381.0212	1.565869	−-2.080	−1.70	−1.92	−1.95[1] , −1.97[2]	−2.08	0.00	0.00	0.00	0.00
TiII	5418.751	1.581911	−1.999	−2.002	−2.00	−2.10[1] , −2.13[2]	−2.13	+0.30	+0.30	+0.30	+0.10

Notes. In Col. 7 literature oscillator strength values are from the references: [(1)] Spite et al. (1987) and [(2)] Wood et al. (2013). Line-by-line abundances for the four sample stars are given.

Table 10. Mean abundances of C, N, odd-*Z* elements Na, Al, and α-elements O, Mg, Si, Ca, Ti.

Star	[C/Fe]	[N/Fe]	[Na/Fe]	[Al/Fe]	[O/Fe]	[Mg/Fe]	[Si/Fe]	[Ca/Fe]	[TiI/Fe]	[TiII/Fe]
B-107	0.00	–	−0.22(+0.03)	−0.30(+0.28)	+0.50	+0.33	+0.17	+0.16	+0.03	+0.17
B-122	−0.20	+0.70	−0.04(+0.09)	−0.20(+0.18)	+0.20	+0.10	+0.06	+0.00	+0.03	+0.15
B-128	0.10	+0.60	+0.01(+0.01)	+0.08(+0.08)	+0.23	+0.23	+0.14	+0.20	+0.05	+0.17
B-130	0.00	+0.70	−0.01(+0.05)	0.00(+0.26)	+0.50	+0.27	+0.13	+0.15	+0.03	+0.18
Mean	−0.03	+0.67	−0.07(+0.05)	−0.11(+0.20)	+0.36	+0.23	+0.13	+0.13	+0.04	+0.17

Notes. For Na and Al the abundance ratios in parenthesis are corrected for a trend with effective temperature.

quadrupole B-factor were adopted from Biehl (1976) and Rutten (1978), as given in Table A.1. The resulting line lists with the HFS for the Ba II 6141.713 and 6496.897 Å lines are given in Table A.2.

Lanthanum: the nuclear spin of the nuclide ^{139}La that contributes with 99.911% to the lanthanum abundance is $I = 7/2$. Hyperfine coupling constants A and B were adopted from Biehl (1976) and Lawler et al. (2001a) as given in Table A.3. For the LaII 6262.287 Å line we adopted the HFS calculation by Van der Swaelmen (2013).

Europium: the nuclear spin of the nuclides ^{151}Eu, and ^{153}Eu is $I = 5/2$, and their isotopic proportions are 47.8% and 52.2% (Lawler et al. 2001b). Hyperfine coupling constants A and B are taken from Lawler et al. (2001b). The HFS splitting was adopted from line lists by Hill et al. (2002), and show a perfect fit to the solar and Arcturus lines. The EuII 6173.029 Å line is too faint in all sample stars, and could not be measured.

For the odd-Z Y no HFS constants were found in the literature. We comment below on lines of Y and Sr used in C11:

Yttrium: the Y I and Y II lines employed are reported in Table 11. The main Y abundance indicator used in C11 was the Y II 6613.733 Å line, and we proceed with a detailed description of this line. The Y II 6613.733 line has a blend with the Fe I 6613.830 Å line, which is 0.097 Å apart. The $\log gf$ values of these two lines given in the literature are too strong, and to be able to use this line, we fitted astrophysical $\log gf$ values. The solar line was fitted to the solar spectrum observed with UVES, and an oscillator strength of $\log gf = -1.2$ was chosen. The blending Fe I 6613.830 Å was fitted with $\log gf = -5.8$. The list of $\log gf$ values around this line is given in Table A.4.

The fitting was then applied to the spectrum of Arcturus using these $\log gf$ values, and was computed with different abundances of yttrium: the [Y/Fe] = −0.3 value assumed from the other Y lines fits the line well, and higher Y abundances

Table 11. Central wavelengths from NIST or Kurúcz line lists and total oscillator strengths from line lists by Kurúcz, NIST, and VALD, the literature, and adopted values.

Species	λ (Å)	χ_{ex} (eV)	gf_{Kurucz}	gf_{NIST}	gf_{VALD}	$gf_{literature}$	$gf_{adopted}$	B-107	B-122	B-128	B-130
EuII	6437.640	1.319712	−0.276	–	−0.320	−0.32[3]	−0.32	+0.45	+0.30	+0.30	+0.30
EuII	6645.064	1.379816	+0.204	–	+0.120	+0.12[3]	+0.12	+0.40	+0.30	+0.30	+0.10
BaII	6141.713	0.703636	−0.076	0.0	−0.076	−0.076	0.00	+0.40	0.0	+0.50	+0.10
FeI	6141.730	3.602	−1.60	–	−1.459	–	−1.60	–	–	–	–
BaII	6496.897	0.604321	−0.377	−0.407	−0.32	–	−0.32	+0.50	+0.10	+0.60	+0.35
LaII	6262.287	0.403019	−1.240	–	−1.220	−1.22[2] , −1.60[5]	−1.60	0.00	+0.40	+0.40	0.00
LaII	6320.376	0.172903	−1.610	–	−1.562	–	−1.56	+0.30	+0.30	+0.30	+0.10
LaII	6390.477	0.321339	−1.450	–	−1.410	−1.41	−1.41	+0.30	+0.30	+0.40	0.00
YII	5473.388	1.738160	−1.02	−1.01	−1.020	−1.02[1]	−1.02	+0.30	+0.15	+0.30	+0.10
YII	5544.611	1.738160	−1.09	−1.08	−1.090	−1.09[1]	−1.09	+0.20	0.00	+0.30	0.00
YII	5546.009	1.748055	−1.10	−1.10	−1.100	−1.10[1]	−1.10	+0.30	+0.30	+0.30	–
YI	6435.004	0.065760	−0.820	−0.83	−0.820	−0.82[1] , −1.07[5]	−0.82	+0.30	0.00	+0.35	–
YII	6613.733	1.011123	−6.689	–	−5.587	–	−5.80	+0.80	+1.00	+1.00	+0.70
FeI	6613.825	1.748055	−1.110	−1.110	−1.110	−1.11[1]	−1.15	–	–	–	–
YII	6795.414	1.738160	−1.190	–	−1.190	–	−1.19	0.00	0.00	+0.30	+0.10
ZrII	5112.270	1.665034	−0.590	–	−0.850	–	−0.59	0.00	+0.10	+0.40	0.00
ZrII	5350.090	1.826828	−1.240	–	−1.240	–	−1.24	–	+0.30	–	–
ZrII	5350.350	1.772925	−1.276	–	−1.160	–	−1.16	+0.30	+0.30	–	–
ZrI	6127.475	0.153855	−1.06	–	−1.060	−1.18[4] , −1.05[5]	−1.18	+0.30	0.00	+0.40	0.00
ZrI	6134.585	0.00	−1.28	–	−1.280	−1.426[4] , −1.28[5]	−1.43	–	0.00	+0.35	–
ZrI	6143.252	0.070727	−1.10	–	−1.100	−1.252[4] , −1.10[5]	−1.50	–	+0.15	+0.30	0.00
SrI	6503.989	2.258995	+0.26	−0.05	+0.320	–	−0.05	0.00	+0.40	0.00	+0.30
SrI	6791.016	1.775266	−0.720	−0.73	−0.73	–	−0.73	–	–	+0.40	–

Notes. In Col. 7, literature oscillator strength values are taken from the references: [(1)] Hannaford et al. (1982); [(2)] Lawler et al. (2001a); [(3)] Lawler et al. (2001b); [(4)] Jacobson & Friel (2013); and [(5)] van der Swaelmen (2013). Line-by-line abundances of heavy elements for the four sample stars are given.

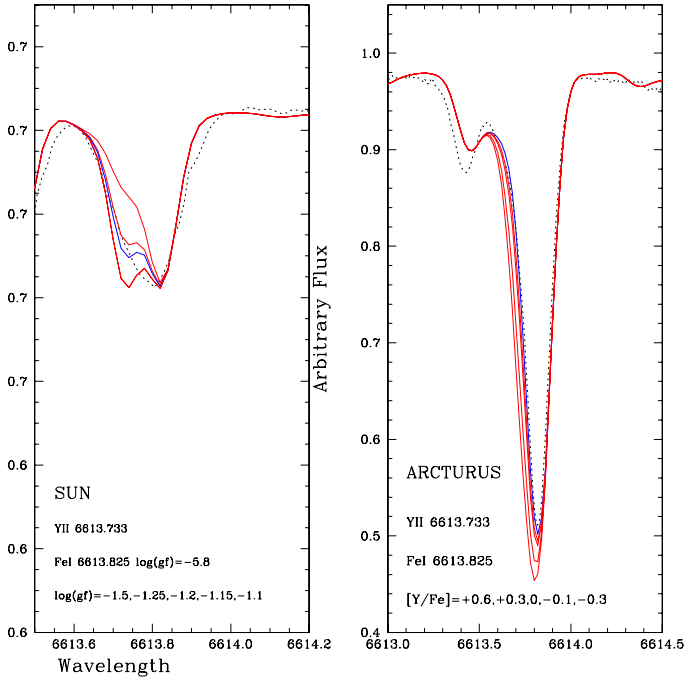

Fig. 7. Y II 6613.733 fittings on the solar and Arcturus spectra. Observed spectra (dashed lines); synthetic spectra (red solid lines); best fit (blue solid line).

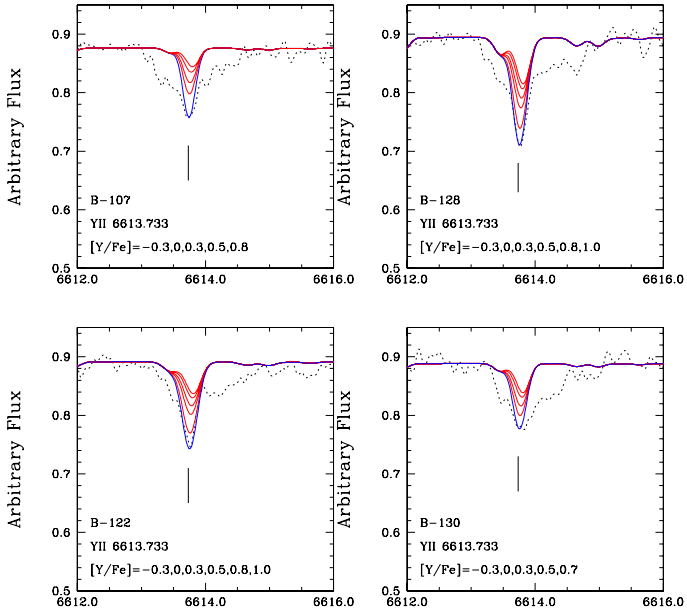

Fig. 8. Y II 6613.733 Å line in the four sample stars, compared with their new UVES spectra. Dotted black line: UVES spectrum; red solid lines: synthetic spectra computed with different [Y/Fe] values as indicated in the panels; blue solid lines correspond to best fits.

will show as a stronger line, whereas a lower Y cannot be seen, only a lower limit is possible in this case. These fits are shown in Fig. 7. On the left wing of the blend Y II 6613.733 + Fe I 6613.830 Å line, there are two additional Ti I 6613.599 and 6613.620 Å lines in the VALD data base that are not given in the Kurúcz line list, with only the Ti I 6613.626 Å given in both data bases. The $\log gf$ of these three Ti I lines were corrected by −0.3 dex, as given in Table A.4 to fit the Arcturus spectrum. The fits to the new UVES spectra are shown in Fig. 8. Even though this line gives higher Y abundances than the other lines,

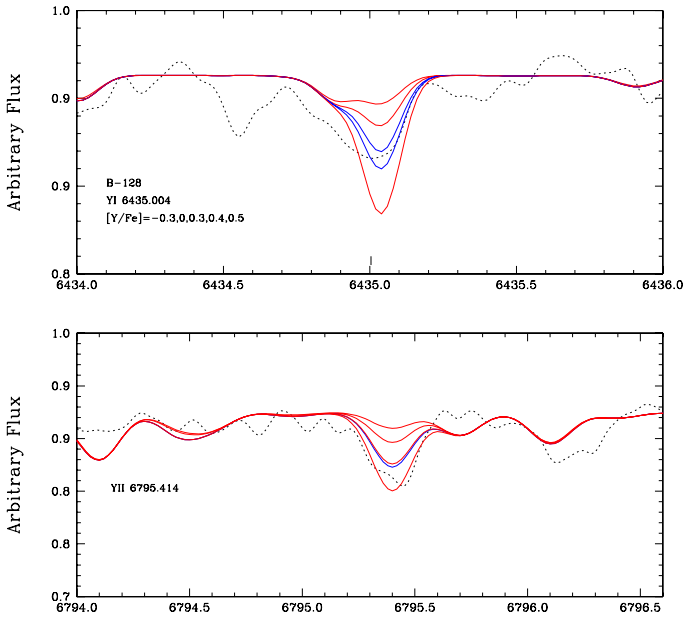

Fig. 9. Y I 6435 andY I 6795 Å lines in B-128. Dotted black line: UVES spectrum; red solid lines: synthetic spectra computed with different [Y/Fe] values as indicated in the panels; blue solid lines: best fits; for the YI 6435 Å line both [Y/Fe] = +0.3 and +0.4 are in blue, and [Y/Fe] = +0.35 was adopted.

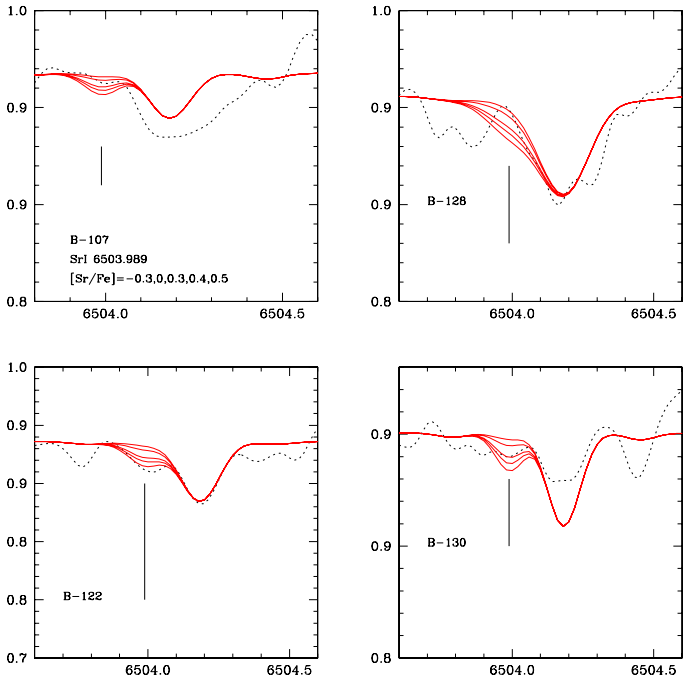

Fig. 10. Sr I 6503.989 Å line in the four sample stars. Symbols: dotted black line: UVES spectrum; red solid lines: synthetic spectra computed with different [Sr/Fe] ratios.

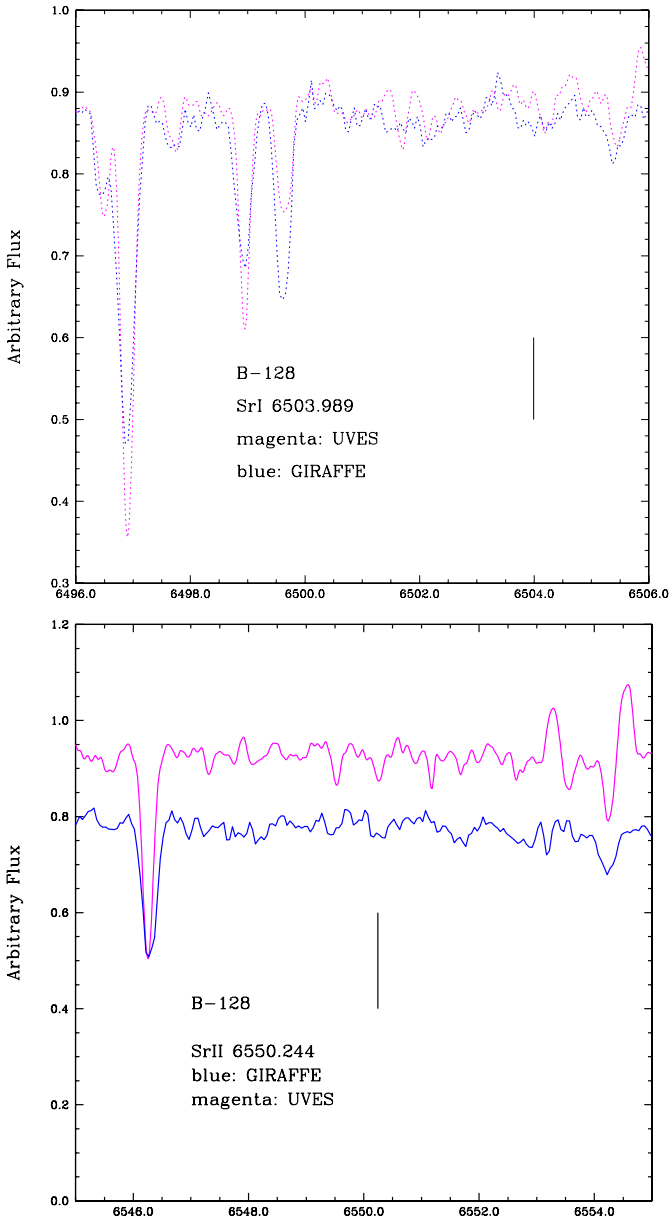

Fig. 11. Sr I 6503.989 and Sr I 6550.244 Å lines in the same star B-128, shown in spectra of UVES from the present work, observed in 2011−2012, and GIRAFFE spectrum studied in B09.

no suitable Y lines are available, therefore the results from this line were taken into account together with the others. Previous GIRAFFE spectra with lower resolution were clearly better fitted with even higher Y abundances.

The fits to Y I 6435 and Y I 6795 Å lines in star B-128 are shown in Fig. 9.

In C11 stronger Y abundances were derived because of a slightly lower $\log gf$ value of the blending Fe I 6613.830 Å line with $\log gf = -5.85$, instead of -5.80, and the Y II 6613.733 line with a $\log gf = -1.25$ instead of -1.20. These lower $\log gf$ values, combined to the lower resolution of the spectra, led to higher Y abundances.

Strontium: the Sr I 6550.244 Å line is blended with nine lines, four of which coincide with the Sr I line (Table A.4), and the $\log gf$ values of these lines, currently listed in the VALD data base, are stronger than the observed lines for the Sun, Arcturus, and the sample stars. We conclude that some of their $\log gf$ values are clearly inaccurate, and since they are blended with each other, it is not possible to derive astrophysical $\log gf$ relative values with confidence. This line was therefore discarded in the present work.

In C11 we used a line list with astrophysically fitted $\log gf$ values, and the lower resolution of the spectra appeared to show a strong SrI 6550 line. Figure 11 shows a comparison of the previous and current spectra for star B-128. The Sr abundances

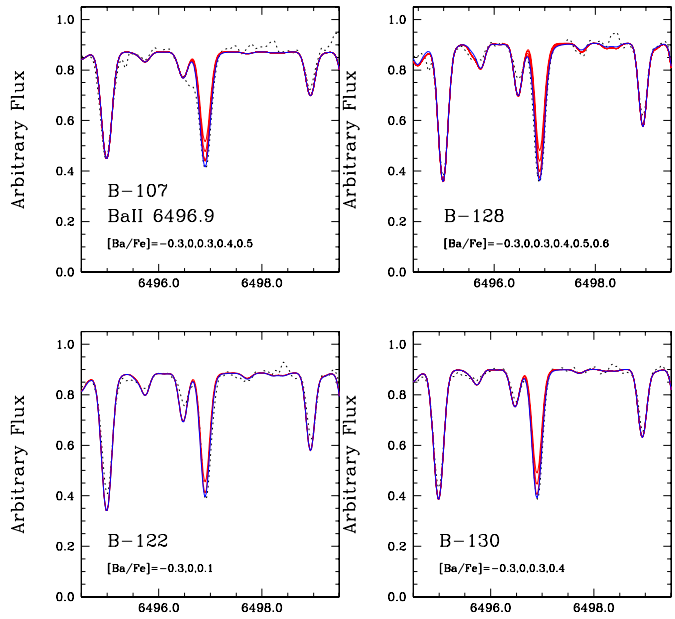

Fig. 12. Ba II 6946 Å line in the four sample stars. Red lines: synthetic spectra computed with several [Ba/Fe] values as indicated in the panels; blue lines: best-fit synthetic spectra.

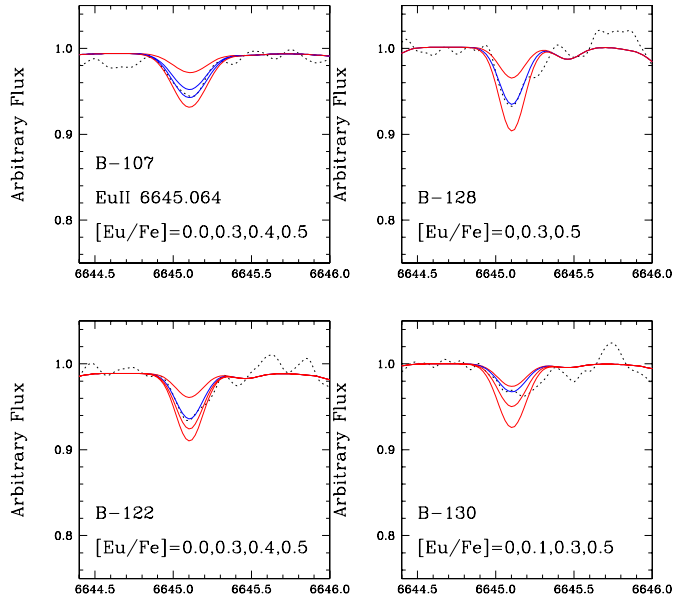

Fig. 13. Eu II 6645 Å line in the four sample stars. Symbols are the same as in Fig. 12.

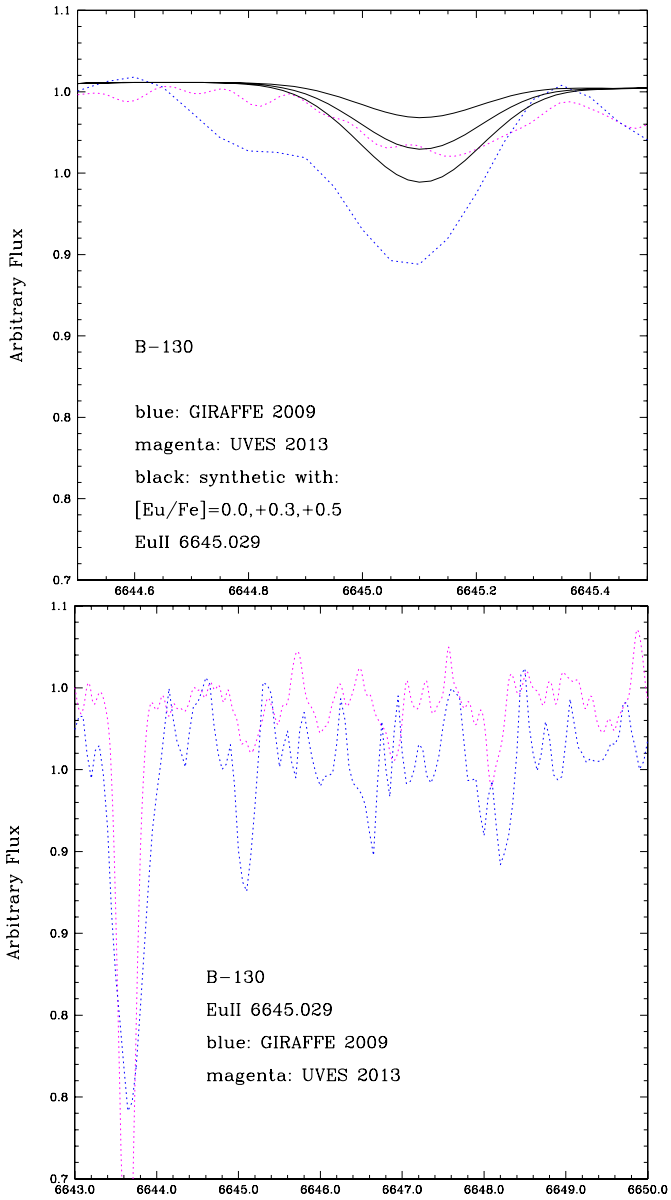

Fig. 14. Eu II 6645 Å line in the same star B-130, shown in spectra of UVES from the present work, observed in 2011−2012, and in the GIRAFFE spectrum studied in B09. *Upper panel*: Eu II 6645 Å line; *lower panel*: the same spectral region enlarged. The magenta dotted line represents the UVES spectrum, the blue dotted line the GIRAFFE spectrum, and the blue solid lines plot the synthetic spectra computed with [Eu/Fe] = 0, +0.3, +0.5.

presented in C11, based on the Sr I 6550.244 Å, should be disconsidered.

Sr I 6503.989 Å instead is relatively unblended, showing a strong line on the red side, for which we derived astrophysical $\log gf$ values (since the VALD $\log gf$ values are again too strong), and blending lines are indicated in Table A.4. This line is the main indicator of the Sr abundance in the present work. Figure 10 shows the Sr I 6503.989 Å line in the four sample stars. There are very few derivations of Sr abundances in bulge stars in the literature, given that the suitable lines are located in the blue part of the spectrum, while in the visible region the lines are faint or blended.

Figures 12 and 13 show the Ba II 6946 Å and Eu II 6645 Å lines in the four sample stars.

To make the differences in Eu abundance from B09, C11, and the present work understandable, we show in Fig. 14 the spectra of star B-130 in the region of the Eu II 6645 Å line obtained with UVES in the present work, observed in 2011−2012, and the HR15 setup of the GIRAFFE spectrum studied in B09. The much stronger noise in the GIRAFFE spectrum with respect to the present UVES spectrum is clearly illustrated, showing that the spectra of the HR15 setup have a lower S/N than previously reported.

In conclusion, given the large uncertainties in the Sr abundances, based on a unique and faint line, we here focus our discussion on Y and Ba, similar to the decision made in C11.

Table 12. Mean heavy element abundances, compared with results from B09 and C11.

Star	[Eu/Fe]	[Eu/Fe]	[Ba/Fe]	[Ba/Fe]	[La/Fe]	[La/Fe]	[Y/Fe]	[Y/Fe]	[Sr/Fe]	[Sr/Fe]	[Zr/Fe]	[Ba/Eu]	[Y/Ba]	[Sr/Ba]
	Old	New	Old	New	Old	New	Old	New	Old	New	New	New	New	New
B-107	0.00	+0.40	+0.50	+0.45	+0.50	+0.20	+1.00	+0.32	+1.30	0.00	+0.20	+0.05	−0.13	−0.45
B-122	+0.30	+0.30	+0.60	+0.05	+0.30	+0.35	+1.20	+0.24	+0.50	+0.40	+0.10	−0.25	+0.19	+0.35
B-128	0.00	+0.30	+0.90	+0.55	–	+0.35	+1.50	+0.43	+1.50	+0.20	+0.40	+0.25	−0.12	−0.35
B-130	+0.80	+0.20	+0.25	+0.22	–	0.00	+1.20	+0.23	–	+0.30	0.00	+0.02	+0.01	+0.08
Mean	–	+0.30	–	+0.32	–	+0.23	–	+0.31	–	+0.23	+0.18	+0.02	−0.01	−0.14

Table 13. Abundance uncertainties for star B-128, for uncertainties of $\Delta T_{\rm eff}$ = 100 K, $\Delta \log g$ = 0.2, $\Delta v_{\rm t}$ = 0.2 km s^{-1} and corresponding total error.

Abundance	ΔT 100 K	$\Delta \log g$ 0.2 dex	$\Delta v_{\rm t}$ 0.2 km s^{-1}	$(\sum x^2)^{1/2}$
(1)	(2)	(3)	(4)	(5)
[FeI/H]	+0.06	0.00	−0.08	0.10
[FeII/H]	−0.07	+0.11	−0.07	0.14
[C/Fe]	+0.02	+0.02	0.00	0.03
[N/Fe]	+0.15	+0.10	0.00	0.18
[O/Fe]	+0.06	0.10	0.00	0.12
[NaI/Fe]	0.00	0.00	0.00	0.00
[Al/Fe]	+0.05	0.00	0.00	0.05
[MgI/Fe]	+0.03	+0.01	0.00	0.02
[SiI/Fe]	+0.01	+0.03	0.00	0.02
[CaI/Fe]	+0.02	−0.02	0.00	0.02
[TiI/Fe]	+0.10	−0.01	0.00	0.10
[TiII/Fe]	0.00	+0.08	−0.02	0.10
[SrI/Fe]	−0.02	0.00	0.00	0.02
[YI/Fe]	+0.15	+0.15	0.00	0.21
[YII/Fe]	+0.20	+0.15	0.00	0.25
[ZrI/Fe]	+0.20	−0.01	0.00	0.20
[BaII/Fe]	+0.10	+0.15	−0.15	0.23
[LaII/Fe]	+0.05	+0.15	0.00	0.16
[EuII/Fe]	0.00	+0.12	0.00	0.12

Notes. The errors are to be added to reach the reported abundances.

6.4. Errors

The errors due to uncertainties in spectroscopic parameters are given in Table 13, applied to the sample star NGC 6522: B-128. The error on the slope in the FeI vs. ionization potential implies an error in the temperature of ±100 K for the sample stars. An uncertainty of the order of 0.2 km s^{-1} on the microturbulence velocity is estimated from the imposition of constant value of [Fe/H] as a function of EWs. Errors are given on FeI and FeII abundances, and other element abundance ratios, induced by a change of $\Delta T_{\rm eff}$ = +100 K, $\Delta \log g$ = +0.2, $\Delta v_{\rm t}$ = 0.2 km s^{-1}, and a total error estimate is given in the last column of Table 13. Additionally, an uncertainty of 0.8 mÅ in EWs of Fe lines yields a metallicity uncertainty of <0.02 dex.

The errors on the abundance ratios [X/Fe] were computed by fitting the lines with the modified atmospheric model. The error given is the abundance difference needed to reach the final abundances reported.

7. Discussion

We derived a mean metallicity of [Fe/H] = −0.95 ± 0.15, which agrees well the results of B09. The final mean abundances are given in Table 10 for C, N, odd-Z elements Na, Al, and the α-elements and in Table 12 for the heavy elements.

To better place the derived abundances in the context of bulge studies, we compare the present results with literature abundances of heavy elements in bulge stars.

Johnson et al. (2012) derived abundances of the heavy elements Zr, La, and Eu in common with our element abundance derivation. Their observations were of red giants in Plaut's field, located at $l = 0°$, $b = -8°$, and $l = -1°$, $b = -8.^{\circ}5$, and their stars have metallicities in the range $-1.6 \leq$ [Fe/H] $\leq +0.5$.

Yong et al. (2014) studied seven stars in the globular cluster M 62 (NGC 6266), located at J(2000) $17^{\rm h}01^{\rm h}12.''80$, $-30°06'49.''4$, $l = 353.^{\circ}57$, $b = 7.^{\circ}32$, therefore projected in the bulge.

Bensby et al. (2013, and references therein) presented element abundances of 58 microlensed bulge dwarfs and subgiants of the Galactic bulge. Their study included the abundances of the heavy elements Y and Ba. Because the authors report ages, including younger stellar populations present in the bulge, we selected a subsample of stars with ages older than 11 Gyr.

In Fig. 15 we plot our results for the heavy elements Sr, Y, Zr, La, Ba, and Eu-over-Fe for the four sample stars (blue squares) compared with literature abundances from Johnson et al. (2012), Yong et al. (2014), and Bensby et al. (2013). This figure indicates that Sr, Y, and Zr are enhanced, and show a spread at [Fe/H] ∼ −1.0, while Ba and La are also enhanced around [Fe/H] ∼ −1.0. These features are compatible with expectations from massive spinstars (see Chiappini 2013).

In M 62, the spread in abundances of Sr, Y, and Zr is consistent with *s*-process production by massive spinstars. On the other hand, the observed [Rb/Y] and partially the [Rb/Zr] seem to disagree with this scenario. The uncertainties of explosive nucleosynthesis in core-collapse supernovae are quite large, and in particular, the spread of [Rb/Zr] and [Rb/Y] in the yields from the SN explosion of spinstars still needs to be explored.

Our results show enhancements of [O/Fe] = +0.36, [Mg/Fe] =≈ +0.23, [Si/Fe] = [Ca/Fe] ≈ +0.13, [TiII/Fe] ≈ +0.17, and lower [TiI/Fe] ≈ +0.04. The *r*-process element Eu is enhanced by [Eu/Fe] = +0.30. The *s*-elements La and Ba are enhanced with [La/Fe] = +0.23 and [Ba/Fe] = +0.32, the latter not as high as the [Ba/Fe] = +0.49 previously found by B09. The odd-*Z* element Na shows essentially a solar ratio with [Na/Fe] ∼ +0.05, and [Al/Fe] = +0.20 with the correction for a trend with effective temperature. Therefore there is no clear indication of a Na-O anticorrelation.

The α-element enhancements in O, Mg together with that of the *r*-process element Eu are indicative of a fast early enrichment by supernovae type II.

When the [Ba/Eu] ratio is considered as indicative of the *s*-process and *r*-process relative contribution, the La and Ba abundances, which are higher than Eu, are not consistent with a pure *r*-process contribution ([Ba/Eu] ∼ 0.0 compared with $[{\rm Ba/Eu}]_{\rm r}$ ∼ −0.8, Bisterzo et al. 2014). Therefore, many of the conclusions discussed by B09 and C11 are still valid.

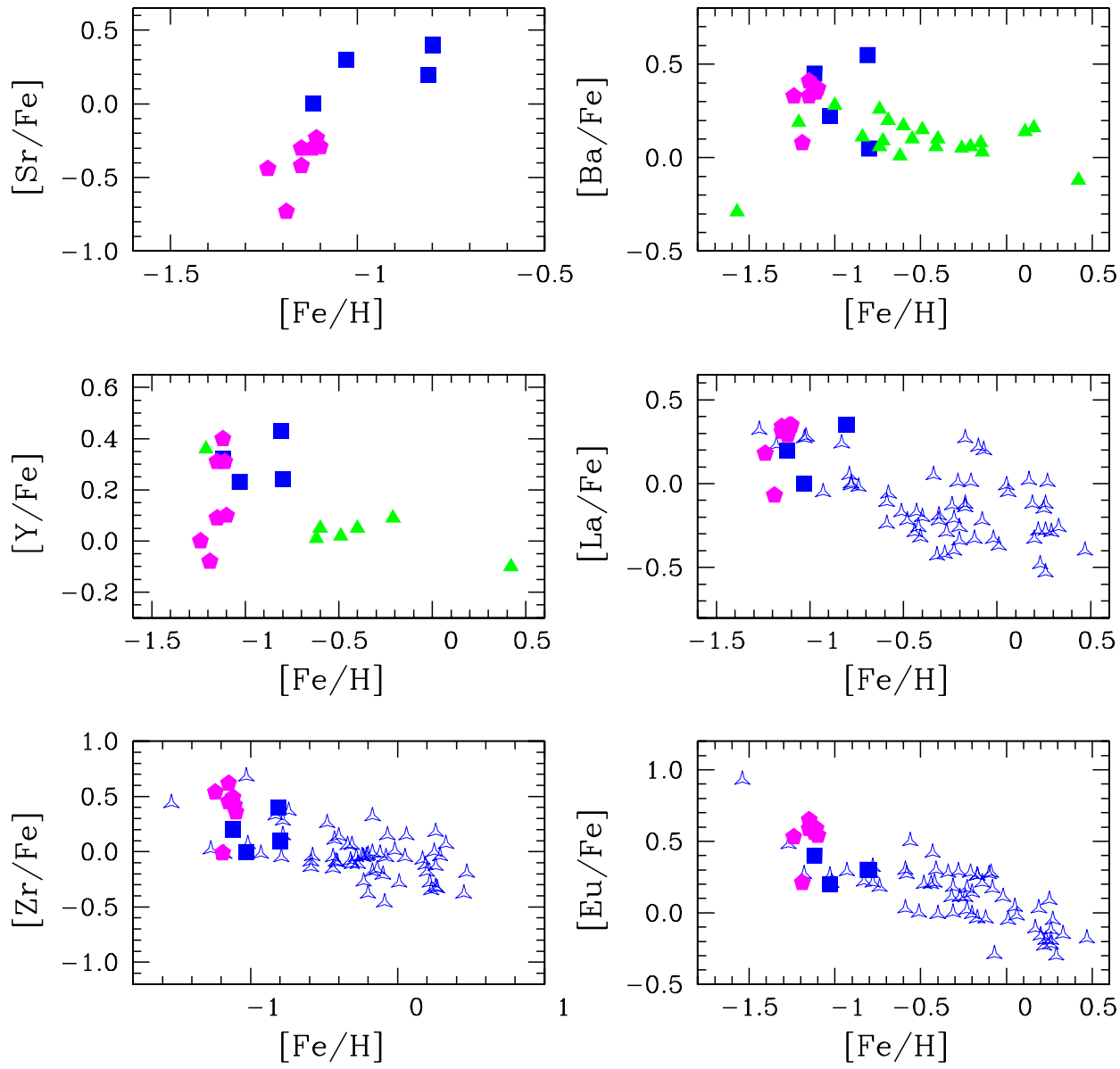

Fig. 15. Sr, Y, Zr, La, Ba, and Eu-over-Fe for the four sample stars (blue filled squares), compared with literature abundances from Johnson et al. (2012) (open triangles), Yong et al. (2014) (magenta filled pentagons), and Bensby et al. (2013) (green filled trianges).

Figure 15 shows the abundances of Sr, Y, Zr, La, Ba, and Eu-over-Fe determined here, compared with other determinations. The data suggest an increase of [Zr/Fe], [Ba/Fe], [La/Fe], and [Eu/Fe] towards low metallicities. For these elements, the abundances measured by different authors for the most metal-poor bulge stars seem to agree with each other (i.e. abundances of field stars from Johnson et al. and Bensby et al., and abundances in the globular clusters NGC 6522 and M 62). The situation seems to be different for Sr and Y. There is still very few measurements in the literature for these elements, especially at metallicities below [Fe/H] $\lesssim -1$. The observations suggest a strong increase in the dispersion of the [Y/Fe] ratios below [Fe/H] < -1 (in particular, there is a large scatter in the [Y/Fe] ratios in the M 62 globular cluster). For Sr the situation is even more unclear, with no determination in bulge field stars, and only a few measurements in NGC 6522 and M 62. However, as discussed in the previous section, our Sr abundances are based only on one very faint line. This might explain the very discrepant measurements we find in NGC 6522 compared with those of M 62. Furthermore, Yong et al. assumed a correction for Non-Local Thermodynamic Equilibrium (NLTE) effects for their [Sr/Fe] of +0.29 dex, using lines in the blue region (their spectra cover the full wavelength region 3800−9000 Å), and we did not take NLTE effects into account in our determinations. For a similar NLTE correction for the stars in NGC 6522, the discrepancy with M 62 stars would be less relevant. We used a different line, which means that the same correction might not apply. Nevertheless, while we cannot discard that the two clusters have different [Sr/Fe] ratios, this possibility seems unlikely since the other measured abundances are consistent, and we qualitatively expect NLTE effects on our line at Sr I 6503 as well. It is important to note that lines in the bluer region are prohibitive in terms of exposure times and expected S/N because our sample stars are faint in the optical and located in rather high extinction regions in the bulge.

Figure 16 shows the [Y/Ba] vs. [Fe/H] diagram. We first focus on the upper panel, where the data plotted are the same sample stars as shown in Fig. 15 (our new four measurements in

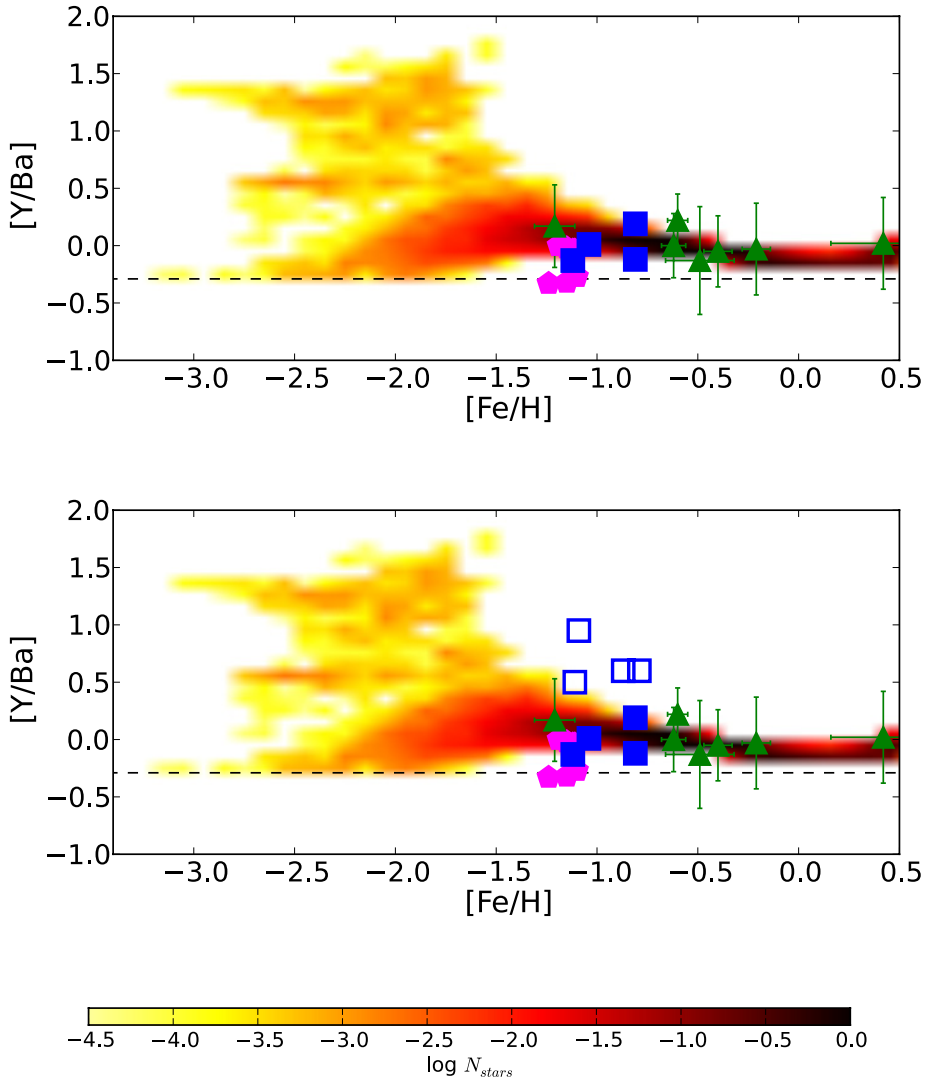

Fig. 16. *Upper panel*: [Y/Ba] vs. [Fe/H] for the four sample stars (blue filled squares) compared with literature abundances from Yong et al. (2014) for M 62 (magenta filled pentagons) and Bensby et al. (2013) for their stars older than 11 Gyr (green filled trianges). We also show chemical evolution model predictions for the bulge (see density scale in the colour bar at the bottom of the figure), where the contribution of both spinstars and magneto-rotationally driven (MRD) supernovae are taken into account (see Chiappini et al. 2014; Cescutti & Chiappini 2014; Cescutti et al. 2013). *Lower panel*: same as the *upper panel*, but now also showing the old abundance values (open blue squares) for the stars for which we have re-obtained better chemical abundances (filled blue squares). The dashed line in both panels corresponds to the *r*-process fractions, which were adopted from Sneden et al. (2008) for metal-poor *r*-element-rich stars. Note that in all panels we have excluded star B-108.

NGC 6522 and the literature data). We also show in this figure a chemical evolution model for the Galactic bulge where the enrichment in heavy elements takes place both in spinstars and in magneto-rotationally driven (MRD) supernovae (Chiappini et al., in prep.; see also Cescutti & Chiappini 2014; Cescutti et al. 2013). As explained in the introduction, at the time C11 was published there were still no available grids of very metal-poor stellar models of fast-rotating spinstars. The situation has now improved and we can now compute chemical evolution models that include the contribution of spinstars also for heavy elements such as Y and Ba. From our most recent model predictions we find that although for the halo the contribution of spinstars leads to a large scatter in the [Y/Ba] ratios around [Fe/H] = −3 (Cescutti et al. 2013; Cescutti & Chiappini 2014), for the bulge the scatter is seen at a lower metallicity around −2 < [Fe/H] < −1. This is particularly true in the case shown here, where the site for the *r*-process is assumed to be MRD supernovae). The main reason for this is the star formation rate in the bulge that is faster than in the halo. More details are reported in Chiappini et al. (in prep.). In the lower panel we also show our old measurements for the re-observed stars. It is clear from this figure that the new chemical abundances obtained here agree better with our model predictions for the bulge. We recall that a good agreement with the [Y/Ba] ratio observed in halo stars is also obtained for a halo model adopting the same nucleosynthesis prescriptions as those adopted in the bulge model shown here (Cescutti & Chiappini 2014). The star B-108 was discarded, as discussed in Sect. 4.2.

As discussed in C11, the *s*-element excesses might be due to an *s*-process enrichment of the primordial matter from which the cluster formed, or to the *s*-process that occurred in nearby AGB stars during He-shell flash episodes, and the ejected material would then have been accreted by the sample stars during their formation process. This latter explanation would also

account for some spread in the Ba abundances, hence offering an alternative explanation to the one involving the existence of spinstars in the early chemical enrichment of the Universe. C11 have shown that for five out of eight studied stars in NGC 6522 both scenarios would work, while for the remaining three stars (with the highest [Y/Ba] ratios) the abundances were not compatible with *s*-process nucleosynthesis in AGB stars, and this indicated that for these the early enrichment due to spinstars might be an option that would have to be investigated by the computation of chemical evolution models when stellar yields for spinstars would be available. Our most recent chemical evolution models for the bulge that include the contribution of spinstars suggest that the previous large enhancements reported in these three stars are incompatible with new calculations for the spinstar scenario. Among these three stars only one (B-130) was re-observed, and its new abundance agrees well with our model predictions. Given this situation, it would be important to try to secure high quality data for the other star F-121 as well. The interpretation that the observed enhancements in La, Ba, Y and Sr in these very old bulge stars are due to early massive spinstars (C11) is still valid, but not anymore unique.

It is important to stress that the suggestions made in C11 opened a new field of evidences concerning bulge stars. Figure 12 shows that at the metallicity around [Fe/H] ~ -1.0, Johnson et al. (2011), Bensby et al. (2013), and Yong et al. (2014) together with our revised results indicate that the *s*-elements [Y/Fe], [Zr/Fe], [Ba/Fe] and [La/Fe] do show significant enhancements. [Sr/Fe] is moderately enhanced in the present stars and deficient in M 62 (Yong et al. 2014), but the abundances for this element are very uncertain. The enhancement of the *r*-element Eu is expected, and confirms that its long-established behaviour is similar to that of α-elements.

8. Conclusions

We present new abundances for four stars in the oldest known MW globular cluster, NGC 6522. The new abundances were obtained from high-resolution UVES spectra with a high S/N. These stars had been studied with lower resolution spectra by Barbuy et al. (2009) and Chiappini et al. (2011). A fifth star, B-108, was found to be displaced relative to the central J2000 coordinates in the OGLE-II catalogue (Udalski et al. 2002), which we verified by comparing them with ACS/HST images, and therefore caution in future studies on bulge stars is recommended. Furthermore, the image shows that there is a blend of two stars, with similar radial velocities. This is confirmed by the asymmetries observed in the new high-resolution UVES spectra. B-108 was finally discarded from the sample because of a clear contamination of its spectrum, and previous abundances for this star cannot be considered either. It would be useful to observe both of these stars and examine whether the abundance enhancements detected in C11 are present. It would be very interesting to obtain high-resolution spectra of star F-121, for which an extremely high [Y/Ba] ratio had been estimated from FLAMES-GIRAFFE spectra in C11, in which only one better stronger line is blended, and other lines are faint. Nevertheless, we would expect that then the new Y measurement will be lower in agreement with the results presented in this work.

The four re-analysed stars now show abundances that are compatible with other recent measurements of heavy elements (Ba, Y, La, Zr, and Eu) in the Galactic bulge (Yong et al. 2014; Bensby et al. 2013; Johnson et al. 2014). An enhancement in *s*-process-dominant elements is found. In particular, the [Y/Ba] ratio of bulge stars in the field (Bensby et al. 2013) or in bulge metal poor globular clusters such as NGC 6522 (this work) and M 62 (Yong et al. 2014) are very similar, and lower than indicated by the FLAMES-GIRAFFE spectra analysed in B09 and C11.

The new abundances agree much better with recent inhomogenous chemical evolution models where spinstars were taken into account. Indeed, the theoretical predictions, which are now possible to compute thanks to the new grid of spinstar models published by Frischknecht et al. (2012), indicate a moderate enhancements of the [Y/Ba] ratio at metallicities [Fe/H] ~ -1.0. The milder enrichment found for Y compared with Ba, and the abundance scatter found for Ba and La makes the mass transfer contribution from *s*-process-rich AGB stars another possible scenario to explain the signature in NGC 6522. The observation of Pb abundance, if feasible, would help to distinguish between these two scenarios, since AGB stars at [Fe/H] ~ -1.0 are also able to efficiently produce Pb.

Acknowledgements. We are grateful to the referee for pertinent and useful comments. B.B., E.C., and M.T. acknowledge grants and fellowships from CNPq, Capes and Fapesp. M.T. acknowledges the FAPESP post-doctoral fellowship No. 2012/05142-5. M.P. acknowledges the support from the Ambizione grant of the SNSF (Switzerland). D.M. acknowledges support from the BASAL Center for Astrophysics and Associated Technologies PFB-06 and FONDECYT Project 1130196. M.Z. acknowledges FONDECYT Project 1110393. D.M. and M.Z. also acknowledge support from the Millennium Institute of Astrophysics MAS IC-12009. S.O. acknowledges the Italian Ministero dell'Università e della Ricerca Scientifica e Tecnologica (MURST), Italy.

References

Alonso, A., Arribas, S., & Martínez-Roger, C. 1998, A&AS, 131, 209
Alonso, A., Arribas, S., & Martínez-Roger, C. 1999, A&AS, 140, 261 (AAM99)
Aoki, W., Suda, T., Boyd, R. N., et al. 2013, ApJ, 766, L13
Asplund, M., Grevesse, N., Sauval, A. J., & Scott, P. 2009, ARA&A, 47, 481
Arcones, A., & Martínez-Pinedo, G. 2011, Phys. Rev. C, 83, 5809
Ballero, S. K., Matteucci, F., Origlia, L., & Rich, R. M. 2007, A&A, 467, 123
Ballester, P., Modigliani, A., Boitquin, O., et al. 2000, The Messenger, 101, 31B
Barbuy, B. 1983, A&A, 123, 1
Barbuy, B., Bica, E., & Ortolani, S. 1998, A&A, 333, 117
Barbuy, B., Perrin, M.-N., Katz, D., et al. 2003, A&A, 404, 661
Barbuy, B., Zoccali, M., Ortolani, S., et al. 2006, A&A, 449, 349
Barbuy, B., Zoccali, M., Ortolani, S., et al. 2007, AJ, 134, 1613
Barbuy, B., Zoccali, M., Ortolani, S., et al. 2009, A&A, 507, 405 (B09)
Bensby, T., Yee, J. C., Feltzing, S., et al. 2013, A&A, 549, A147
Bessell, M. S. 1979, PASP, 91, 589
Biehl, D. 1976, Ph.D. Thesis, Kiel University, Germany
Bisterzo, S., Travaglio, C., Gallino, R., et al. 2014, ApJ, 787, 10
Carpenter, J. M. 2001, AJ, 121, 2851
Carretta, E., Bragaglia, A., Gratton, R., & Lucatello, S. 2009, A&A, 505, 139
Cayrel, R. 1988, in The Impact of Very High S/N Spectroscopy on Stellar Physics, eds. G. Cayrel de Strobel, & M. Spite, IAU Symp., 132, 345
Cayrel, R., Depagne, E., Spite, M., et al. 2004, A&A, 416, 1117
Cescutti, G., Chiappini, C., Hirschi, R., Meynet, G., & Frischknecht, U. 2013, A&A, 553, A51
Cescutti, G., & Chiappini, C. 2014, A&A, 565, A51
Chiappini, C. 2013, Astron. Nachr., 334, 595
Chiappini, C., Hirschi, R., Meynet, G., et al. 2006, A&A, 449, L27
Chiappini, C., Frischknecht, U., Meynet, G., et al. 2011, Nature, 472, 454 (C11)
Coelho, P., Barbuy, B., Meléndez, J., Schiavon, R. P., & Castilho, B. V. 2005, A&A, 443, 735
Dean, J. F., Warpen, P. R., & Cousins, A. J. 1978, MNRAS, 183, 569
Dékány, I., Minniti, D., Catelan, M., et al. 2013, ApJ, L19
Dekker, H., D'Odorico, S., Kaufer, A., Delabre, B., & Kotzlowski, H. 2000, SPIE, 4008, 534D
Frischknecht, U., Hirschi, R., & Thielemann, F.-K. 2012, A&A, 538, L2
Gopka, V. F., Yushchenko, A. V., Mishenina, T. V., & Kovtyukh, V. V. 2001, Odessa Astron. Pub., 14, 237
Goriely, S., Sida, J.-L., Lemaître, J.-F., et al. 2013, Phys. Rev. Lett., 111, 2502
Gratton, R. G., Carretta, E., & Bragaglia, A. 2012, A&ARv, 20, 50
Grevesse, N., & Sauval, J. N. 1998, Space Sci. Rev., 35, 161
Grevesse, M., Scott, N., Asplund, P., & Sauval, A. J. 2014, A&A, in press, DOI: 10.1051/0004-6361/201424111

Gustafsson, B., Edvardsson, B., Eriksson, K., et al. 2008, A&A, 486, 951
Hannaford, P., Lowe, R. M., Grevesse, N., et al. 1982, ApJ, 261, 736
Hansen, C. J., Bergemann, M., Cescutti, G., et al. 2013, A&A, 551, A57
Harris, W. E. 1996, AJ, 112, 1487
Hinkle, K., Wallace, L., Valenti, J., & Harmer, D. 2000, Visible and Near Infrared Atlas of the Arcturus Spectrum 3727−9300 A, eds. K. Hinkle, L. Wallace, J. Valenti, & D. Harmer (San Francisco: ASP)
Hill, V., Plez, B., Cayrel, R., et al. 2002, A&A, 387, 560
Jacobson, H. R., & Friel, E. 2013, ApJ, 145, 107
Johnson, C. I., Rich, R. M., Kobayashi, C., & Fulbright, J. P. 2012, ApJ, 749, 175
Kurúcz, R. 1993, CD-ROM 23 (Cambridge, Mass: Smithsonian Astrophysical Observatory)
Lawler, J. E., Bonvallet, G., & Sneden, C. 2001a, ApJ, 556, 452
Lawler, J. E., Wickliffe, M. E., Den Hartog, E. A., & Sneden, C. 2001b, ApJ, 563, 1075
Lee, Y.-W. 1992, AJ, 104, 1780
Lodders, K., Palme, H., Gail, H.-P. 2009, Landolt-Börnstein – Group VI Astronomy and Astrophysics Numerical Data and Functional Relationships in Science and Technology Vol. 4B: Solar System, ed. J. E. Trümper, 4.4., 44
Luck, R. E., & Heiter, U. 2005, AJ, 129, 1063
Mäckle, R., Holweger, H., Griffin, R., & Griffin, R. 1975, A&A, 38, 239
Martin, W. C., Fuhr, J. R., Kelleher, D. E., et al. 2002, NIST Atomic Database, version 2.0, National Institute of Standards and Technology, Gaithersburg, MD, http://physics.nist.gov/asd
McWilliam, A., & Rich, R. M. 1994, ApJS, 91, 749
Meléndez, J., & Barbuy, B. 2009, A&A, 497, 611
Meléndez, J., Barbuy, B., Bica, E., et al. 2003, A&A, 411, 417
Minniti, D. 1995, AJ, 109, 1663
Mishenina, T. V., & Kovtyukh, V. V. 2001, A&A, 370, 951
Mishenina, T. V., Panchuk, V. E., & Samus, N. N. 2003, Astron. Rep., 47, 248
Modigliani, A., Mulas, G., Porceddu, I., et al. 2004, The Messenger, 118, 8
Nakamura, K., Kajino, T., Mathews, G., et al. 2013, IJMPE, 2230022
Ness, M., Debattista, V. P., Bensby, T., et al. 2014, ApJ, 787, L19
Peterson, R. C., Dalle Ore, C. M., & Kurúcz, R. 1993, ApJ, 404, 333
Phillips, J. G., & Davis, S. P. 1968, The Swan system of the C_2 molecule (Univ. of California Press)
Pignatari, M., Gallino, R., Meynet, G., et al. 2008, ApJ, 687, L95
Piskunov, N., Kupka, F., Ryabchikova, T., et al. 1995, A&AS, 112, 525
Prochaska, J. X., & McWilliam, A. 2000, ApJ, 537, L57
Rich, R. M., Ortolani, S., Bica, E., & Barbuy, B. 1998, AJ, 116, 1295
Rieke, G. H., & Lebofsky, M. J. 1985, ApJ, 288, 618
Rutledge, G. A., Hesser, J. E., Stetson, P. B., et al. 1997a, PASP, 109, 883
Rutledge, G. A., Hesser, J. E., & Stetson, P. B. 1997b, PASP, 109, 907
Rutten, R. J. 1978, Sol. Phys., 56, 237
Qian, Y.-Z. 2012, AIPC, 1484, 201
Saito, R., et al. (VVV collaboration) 2012, A&A, 537, A107
Simmerer, J., Sneden, C., Cowan, J. J., et al. 2004, ApJ, 617, 1091
Skrutskie, M., Cutri, R. M., Stiening, R., et al. 2006, AJ, 131, 1163
Sneden, C., Cowan, J. J., & Gallino, R. 2008, ARA&A, 46, 241
Spite, M. 1967, Ann. Ap., 30, 211
Spite, M., Huille, S., François, P., & Spite, F. 1987, A&AS, 71, 591
Soto, M., Barbá, R., Gunthardt, G., et al. 2013, A&A, 552, A101
Stetson, P. B., & Pancino, E. 2008, PASP, 120, 1332
Terndrup, D. M., Popowski, P., Gould, A., et al. 1998, AJ, 115, 1475
Truran, J. W. 1981, A&A, 97, 391
Udalski, A., Szymański, M., Kubiak, M., et al. 2002, Acta. Astron., 52, 217
van der Swaelmen, M. 2013, A&A, 560, A44
Wanajo, S. 2013, ApJ, 770, L22
Winteler, C., Käppeli, R., Perego, A., et al. 2012, ApJ, 750, L22
Wood, M. P., Lawler, J. E., Sneden, C., & Cowan, J. J. 2013, ApJS, 208, 27
Yong, D., Alves-Brito, A., Da Costa, G., et al. 2014, MNRAS, 439, 2638
Zacharias, N., Finch, C. T., Girard, T. M., et al. 2013, AJ, 145, 44
Zoccali, M., Barbuy, B., Hill, V., et al. 2004, A&A, 423, 507
Zoccali, M., Lecureur, A., Barbuy, B., et al. 2006, A&A, 457, L1
Zoccali, M., Lecureur, A., Hill, V., et al. 2008, A&A, 486, 177

Pages 18 to 21 are available in the electronic edition of the journal at http://www.aanda.org

Appendix A: Equivalent widths and atomic data

In Table A.1 we list the hyperfine structure constants for the BaII 6141.713 and 6496.897 Å lines, in Table A.2 the list of lines substructured because of the hyperfine structure. In Table A.3 we list the hyperfine structure constants for LaII lines studied in this work.

In Table A.4 we report the lines that blend and overlap Sr I 6503.989, 6550.244 Å, and Y II 6613.733.

Table A.5 presents the equivalent widths of FeI and FeII lines used in the analysis. In Fig. A.1 we plot the EWs measured in the UVES spectra in 2014 (EW(2014)) vs. EWs measured in the GIRAFFE spectra in 2009 (EW(2009)), and residuals between the two. For star B-108, we also compare the measurements with IRAF on the UVES spectra and with EW(2009). The better de-blending of lines with IRAF from the probable presence of two stars explains the poor fit between IRAF and the other EWs.

Table A.1. Atomic constants for BaII used to compute the hyperfine structure: A constants are taken from Rutten (1978), B constants from Biehl (1976), and when the B constants were not available in the literature we assumed them to be null.

Species	λ (Å)	Lower level	J	A(mK)	A(MHz)	B(mK)	B(MHz)	Upper level	J	A(mK)	A(MHz)	B(mK)	B(MHz)
^{135}BaII	6141.713	5d $^2D_{5/2}$	5/2	1.49	44.6691	0	0	6p $^2P^\circ_{3/2}$	3/2	+3.47	104.028	+2.2	65.9544
^{137}BaII	6141.713	5d $^2D_{5/2}$	5/2	1.66	49.7655	0	0	6p $^2P^\circ_{3/2}$	3/2	+3.88	116.3195	+3.25	97.4326
^{135}BaII	6496.897	5d $^2D_{3/2}$	3/2	3.56	106.7261	0	0	6p $^2P^\circ_{1/2}$	1/2	+21.7	650.5497	0	0
^{137}BaII	6496.897	5d $^2D_{3/2}$	3/2	3.97	119.0176	0	0	6p $^2P^\circ_{1/2}$	1/2	+24.2	725.4979	0	0

Table A.2. Hyperfine structure for Ba II lines. log gf adopted: fitting on solar and Arcturus spectra.

6141.713 Å; χ = 0.7036 eV log gf(total) = 0.0			6496.897 Å; χ = 0.6043 eV log gf(total) = −0.32		
λ (Å)	log gf	iso	λ (Å)	log gf	iso
6141.713	−1.617	134	6496.897	−1.937	134
6141.709	−2.385	135	6496.903	−2.704	135
6141.709	−2.431	135	6496.904	−2.306	135
6141.708	−3.385	135	6496.886	−3.005	135
6141.712	−2.063	135	6496.907	−2.306	135
6141.710	−2.318	135	6496.889	−2.306	135
6141.705	−3.561	135	6496.894	−1.858	135
6141.714	−1.813	135	6496.897	−1.425	136
6141.709	−2.415	135	6496.903	−2.475	137
6141.715	−1.607	135	6496.905	−2.077	137
6141.713	−1.105	136	6496.885	−2.776	137
6141.713	−2.154	137	6496.909	−2.077	137
6141.713	−2.200	137	6496.888	−2.077	137
6141.712	−3.154	137	6496.893	−1.630	137
6141.714	−1.832	137	6496.897	−0.464	138
6141.713	−2.087	137			
6141.707	−3.330	137			
6141.715	−1.582	137			
6141.709	−2.184	137			
6141.711	−1.376	137			
6141.713	−0.144	138			

Table A.3. Atomic constants for LaII used to compute hyperfine structure: A and B constants are from Lawler et al. (2001a) and Biehl (1976), and where the B constants were not available in the literature, we assumed them as null.

Species	λ (Å)	Lower level	J	A(mK)	A(MHz)	B(mK)	B(MHz)	Upper level	J	A(mK)	A(MHz)	B(mK)	B(MHz)
^{139}LaII	6262.287	d6s a3D	4.0	–	–	–	–	d4f y3F	3.0	4.959	148.67	0.15	4.5
^{139}LaII	6320.376	d6s a1D	2.0	31.649	948.81	1.66	49.77	d4f y3F	2.0	12.204	365.87	−0.13	–3.90
^{139}LaII	6390.477	d6s a3D	2.0	–37.6	–1127.22	1.66	49.77	d4f y3F	3.0	4.959	148.67	0.15	4.5

Table A.4. Blends near and overlapping the Sr I 6503.989, 6550.244 Å, and Y II 6613.733 lines.

Species	λ (Å)	χ_{ex} (eV)	gf_{Kurucz}	gf_{NIST}	gf_{VALD}	$gf_{adopted}$
VI	6503.757	3.567	−4.641	–	−4.641	−4.641
Fe1	6503.796	5.345	–	–	−8.813	−8.813
Sc2	6503.880	7.439	−2.240	–	−2.240	−2.240
Tm2	6503.930	3.715	–	–	−2.490	−2.490
Fe1	6503.974	5.538	–	–	−4.97	−4.970
Ce1	6503.977	0.493	−1.661	–	−1.661	−1.661
Sr1	6503.989	2.258	+0.260	−0.050	+0.320	+0.320
Ni1	6504.063	5.363	−2.215	–	−2.415	−2.415
Pr1	6504.066	1.291	−0.217	–	−0.217	−0.217
Ce1	6504.125	0.517	−1.637	–	−1.637	−1.637
V1	6504.164	1.183	−1.230	−1.230	−1.23	−1.230
Fe1	6504.182	4.733	−0.357	–	−3.425	−3.425
Co1	6504.210	3.687	−1.737	–	−1.737	−2.437
Mn2	6550.103	4.779	−6.804	–	−6.804	−6.804
Cr1	6550.135	3.369	−4.185	–	−4.185	−4.185
Nd2	6550.178	0.321	−2.280	–	−1.850	−1.850
Ca1	6550.217	5.049	−1.007	–	−2.107	−2.107
Fe2	6550.227	4.837	–	–	−6.086	−6.086
Fe2	6550.249	9.761	–	–	−4.468	−4.468
Sc2	6550.253	7.482	+0.611	–	+0.611	+0.611
Ni1	6550.355	5.363	−1.417	–	−2.117	−2.117
Si1	6550.365	6.083	–	–	−2.852	−2.852
SrI	6550.244	2.690	+0.180	+0.460	+0.180	+0.180
Ce2	6613.392	4.014	–	–	−3.090	−1.590
Fe1	6613.502	5.538	–	–	−4.412	−3.412
Ti1	6613.599	3.718	–	–	−2.025	−2.325
Ti1	6613.620	2.495	–	–	−2.443	−2.743
Ti1	6613.626	1.460	−2.736	–	−3.101	−3.401
V2	6613.632	9.342	–	–	−2.796	−2.796
Fe2	6613.709	12.199	–	–	−5.695	−5.695
Y2	6613.730	1.748	−1.110	−1.110	−1.110	−1.200
Cr2	6613.776	11.234	–	–	+0.515	+0.515
Fe1	6613.825	1.011	−6.689	–	−5.587	−5.800
Ca1	6613.899	5.882	−3.654	–	−3.654	−2.654

Table A.5. Fe I and Fe II lines employed, their wavelengths, excitation potential (eV), oscillator strengths adopted from B09, and equivalent widths as given in B09 from GIRAFFE spectra, and those we measured with the code DAOSPEC on UVES spectra. For star B-108 we also measured EWs with IRAF.

Species	λ(Å)	χ_{ex}	log gf	B-107		B-108			B-122		B-128		B-130	
	Å	(eV)		B09	DAO	B09	DAO	IRAF	B09	DAO	B09	DAO	B09	DAO
FeII	6149.26	3.89	−2.69	31	29.6	22	49.9	18.6	25	43.1	31	36.1	32	36.3
FeII	6247.56	3.89	−1.98	51	44.3	25	15.7	23.4	42	25.1	44	26.2	43	–
FeII	6432.68	2.89	−3.57	42	38.0	28	24.7	17.7	33	38.2	38	32.3	38	37.2
FeII	6456.39	3.90	−2.05	76	73.6	49	53.6	20.9	53	60.2	51	57.0	53	56.4
FeII	6516.08	2.89	−3.31	53	64.2	34	33.3	32.4	44	–	44	47.7	43	44.9
FeI	6151.62	2.18	−3.299	44	42.9	52	80.3	35.0	59	81.8	68	77.1	52	70.1
FeI	6159.38	4.61	−1.97	–	11.6	–	–	2.4	–	–	–	18.8	13	–
FeI	6165.36	4.14	−1.549	23	24.1	–	59.1	9.0	–	54.0	29	51.1	25	43.8
FeI	6173.34	2.22	−2.879	67	65.8	62	94.2	38.2	88	111.9	92	103.1	78	91.3
FeI	6180.20	2.73	−2.784	44	42.7	50	78.8	33.1	58	83.6	70	70.0	60	67.3
FeI	6187.99	3.94	−1.718	22	26.1	21	49.8	9.0	27	44.7	34	43.1	31	36.6
FeI	6200.31	2.61	−2.437	64	64.0	66	75.6	31.2	73	91.3	81	89.2	76	81.3
FeI	6213.43	2.22	−2.646	87	88.4	78	85.0	43.7	96	107.1	98	107.5	91	95.1
FeI	6220.78	3.88	−2.460	11	8.9	–	–	6.0	–	–	–	13.1	–	–
FeI	6226.74	3.88	−2.202	16	8.2	–	6.4	9.0	16	9.2	17	11.6	15	7.8
FeI	6240.65	2.22	−3.388	86	36.8	45	24.6	31.4	57	51.1	73	60.0	50	45.3
FeI	6246.32	3.60	−0.956	86	82.7	73	57.6	68.8	95	84.8	110	86.2	100	67.4
FeI	6252.56	2.40	−1.687	117	115.0	103	17.0	72.3	116	109.6	118	111.1	119	106.7
FeI	6254.25	2.28	−2.480	103	94.1	87	47.2	55.6	108	101.8	116	106.3	106	91.6
FeI	6270.23	2.86	−2.711	36	41.8	51	40.7	40.4	60	61.0	72	62.1	62	43.4
FeI	6271.28	3.32	−2.957	9	15.3	18	–	18.6	–	10.3	12	10.6	–	7.4
FeI	6297.79	2.22	−2.740	58	77.0	63	–	42.6	75	76.7	90	89.9	72	73.2
FeI	6301.50	3.65	−0.720	90	89.5	67	83.7	46.6	84	–	86	100.9	90	88.9
FeI	6302.50	3.69	−0.91	75	65.6	66	65.8	55.0	72	82.4	88	84.5	79	72.4
FeI	6311.50	2.83	−3.224	28	–	38	34.7	24.0	43	–	46	40.1	44	35.3
FeI	6315.31	4.14	−1.230	42	27.9	33	39.7	33.5	42	50.2	48	50.8	33	42.1
FeI	6315.81	4.14	−1.712	30	21.2	30	31.4	20.8	42	–	39	37.0	30	30.5
FeI	6322.69	2.59	−2.426	69	64.9	59	61.6	42.7	77	84.4	89	86.0	70	76.7
FeI	6335.33	2.20	−2.229	106	97.7	90	102.6	66.8	110	118.7	120	118.3	103	112.6
FeI	6336.82	3.69	−1.053	77	77.9	70	82.6	56.8	80	102.0	–	96.7	69	92.3
FeI	6344.15	2.43	−2.922	56	52.4	55	73.7	35.7	75	88.0	84	83.7	65	72.6
FeI	6355.03	2.84	−2.40	35	54.2	58	76.1	34.9	80	98.4	94	98.6	70	78.4
FeI	6392.54	2.28	−4.03	–	6.5	–	36.1	10.9	18	27.7	24	26.9	31	22.9
FeI	6393.60	2.43	−1.615	136	118.0	107	131.0	97.	123	147.1	152	143.9	143	135.2
FeI	6419.95	4.73	−0.250	41	38.9	47	54.5	28.1	53	69.7	62	65.1	53	52.8
FeI	6430.85	2.18	−2.005	112	115.0	116	112.3	80.2	121	131.4	133	130.3	124	117.3
FeI	6475.62	2.56	−2.94	42	54.7	57	61.5	43.3	57	68.9	64	68.4	61	53.9
FeI	6481.87	2.28	−2.984	58	61.7	64	54.1	50.8	72	71.0	78	77.2	74	67.8
FeI	6498.94	0.96	−4.699	44	48.0	74	51.4	34.6	68	74.9	73	74.1	70	63.8
FeI	6518.37	2.83	−2.748	46	40.5	45	42.6	31.7	60	61.2	61	57.9	48	50.2
FeI	6533.93	4.56	−1.453	19	–	–	–	–	25	–	–	–	25	–
FeI	6569.22	4.73	−0.422	38	41.4	49	67.4	26.2	52	68.9	69	64.4	62	54.1
FeI	6574.23	0.99	−5.042	18	29.4	41	56.4	32.5	49	69.6	50	63.9	45	50.0
FeI	6575.02	2.59	−2.824	47	42.1	57	59.5	34.4	69	77.5	79	73.6	64	65.1
FeI	6591.31	4.59	−2.06	–	–	–	13.5	4.2	–	–	9	–	–	–
FeI	6593.87	2.43	−2.422	86	76.4	86	84.8	57.1	98	107.0	105	103.0	87	98.9
FeI	6597.56	4.80	−1.061	13	–	21	–	–	31	24.5	34	–	17	–
FeI	6608.03	2.28	−4.038	7	–	–	18.4	8.4	25	23.5	15	22.2	13	17.0
FeI	6678.00	2.69	−1.420	118	118.8	–	106.1	78.5	139	135.1	148	135.6	134	116.9
FeI	6703.57	2.76	−3.15	35	24.8	28	26.7	17.6	37	39.9	54	40.7	19	33.5
FeI	6705.11	4.61	...	–	17.7	–	12.4	–	12	23.6	40	22.3	26	16.6
FeI	6710.32	1.48	−4.874	14	16.8	–	46.9	13.5	31	30.9	46	34.3	32	20.1
FeI	6713.75	4.80	−1.602	–	5.3	–	14.4	4.0	–	–	–	8.1	5	–
FeI	6715.38	4.59	−1.638	17	10.7	–	27.1	–	12	–	27	14.5	18	6.9
FeI	6716.24	4.56	−1.927	11	–	–	55.2	–	8	–	31	–	10	–
FeI	6725.36	4.10	−2.300	–	–	–	32.5	–	10	5.0	5	–	20	–
FeI	6726.67	4.59	−1.090	–	10.5	27	80.3	–	34	17.9	18	19.3	32	16.5
FeI	6733.15	4.64	−1.576	22	13.1	–	–	–	27	–	31	17.9	18	6.9
FeI	6739.52	1.56	−4.941	–	–	–	59.1	–	36	24.6	25	19.7	25	17.7
FeI	6752.71	4.64	−1.366	27	9.7	–	94.2	–	28	30.0	23	22.7	6	13.5

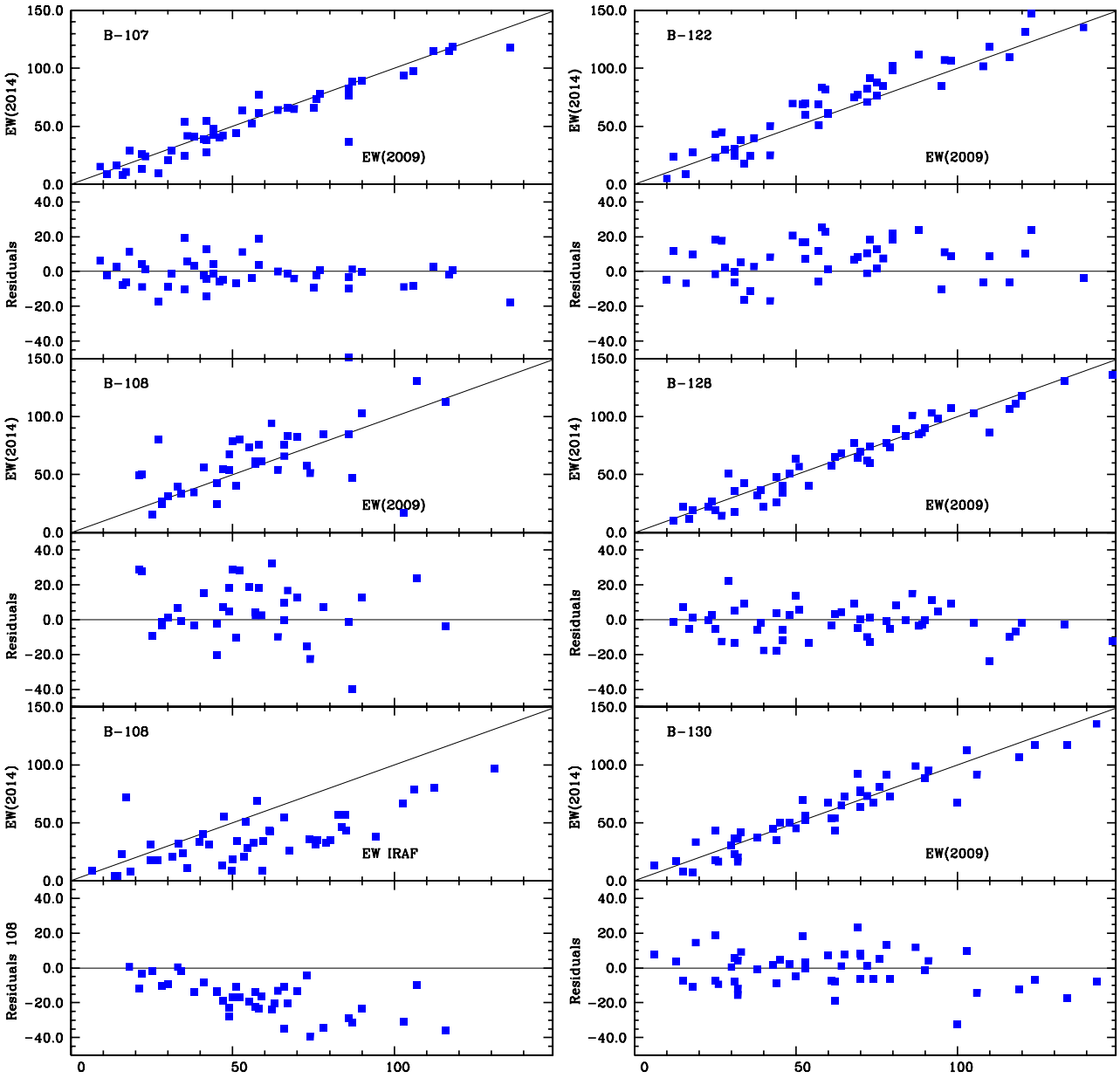

Fig. A.1. Equivalent widths measured in the UVES spectra in 2014 (EW(2014)) vs. equivalent widths measured in the GIRAFFE spectra in 2009 (EW(2009)), and residuals between the two. For each star the *upper panel* gives EW(2014) vs. EW(2009), and the *lower panel* gives the residuals. For star B-108, also the measurements with IRAF on the UVES spectra are compared with EW(2009).